Modeling Soot Formation from Solid Complex Fuels[☆]

Alexander J. Josephson[a,b], Rod R. Linn[b], David O. Lignell[a,*]

[a] *Department of Chemical Engineering, Brigham Young University, Provo, UT, 84602*
[b] *Earth and Environmental Sciences Division, Los Alamos National Laboratory, Los Alamos, NM, 87544*

Abstract

A detailed model is proposed for predicting soot formation from complex solid fuels. The proposed model resolves two particle size distributions, one for soot precursors and another for soot particles. The precursor size distribution is represented with a sectional approach while the soot particle-size distribution is represented with the method of moments and an interpolative closure method is used to resolve fractional methods. Based on established mechanisms, this model includes submodels for precursor coagulation, growth, and consumption, as well as soot nucleation, surface growth, agglomeration, and consumption. The model is validated with comparisons to experimental data for two systems: coal combustion over a laminar flat-flame burner and biomass gasification. Results are presented for soot yield for three coals at three temperatures each, and for soot yield from three types of biomass at two temperatures each. These results represent a wide range of fuels and varying combustion environments, demonstrating the broad applicability of the model.

Keywords: soot formation, coal, biomass, method of moments

1. Introduction

The formation of soot is a well-studied phenomena but still an active area of research [1]. Most research in soot formation processes have focused on soot formed from gaseous fuels, and sophisticated detailed-models have been developed to predict soot concentrations in these types of systems [2, 3, 4, 5, 6, 7, 8, 9]. Soot models tend to follow a series of observed mechanism steps: particle nucleation, coagulation, surface growth, aggregation, and oxidation.

In gaseous fuels, poly-cyclic aromatic hydrocarbons (PAH) act as soot precursors. PAHs are formed in fuel-rich regions where radical gas species are in high enough concentrations to facilitate the formation of aromatic rings [10]. Small aromatics grow through various chemical mechanisms to form larger PAHs. Once PAHs are of sufficient size, they nucleate

[☆] As applied to wood and coal combustion

[*] Corresponding author

Email addresses: alexanderj@lanl.gov (Alexander J. Josephson), rrl@lanl.gov (Rod R. Linn), davidlignell@byu.edu (David O. Lignell)

forming soot nuclei. Once nuclei are formed, particles grow through surface-gas reactions and particle-particle coagulation [4, 11]. Small particles are roughly spherical; but as particles grow larger, they will begin to aggregate into chain-like structures [12].

Soot formation processes for solid fuel combustion differ from gaseous fuel [13]. This is because during the primary pyrolysis of complex solid fuels, such as wood or coal, a large variety of volatile species are released from the parent fuel into the surroundings. Some of these species, often referred to as tars, are large molecules and aromatic in nature. These tars have a tendency to serve as primary soot precursors [14]. As opposed to PAHs from gaseous fuels, tar molecules may have aliphatic portions and inorganic elements attached to the aromatic clusters reflecting the composition of the parent fuel, thus altering the fundamental chemistry of the molecule [15]. The soot formation processes in these solid-complex fuel environments are not as well studied as for gaseous fuels, and there exist only a few predictive models for these systems [16, 17, 18, 19]. These existing models contain system-specific and fuel-specific empirical calibrations and are limited in their extended application.

This study presents a physics-based detailed model for predicting soot formation from complex-solid fuels along with two validation cases, one using coal and the other using biomass. Effects of soot on combustion systems (radiative properties, combustion efficiency, etc) are most closely linked to the soot volume fraction which may be derived from a particle size distribution (PSD) resolved by this model. Results of the proposed model are compared against measured soot concentrations.

2. Model Development

As described in the introduction, soot formation is dependent on the presence of soot precursors and the transformation of soot particles throughout a system. The proposed model describes PSDs and their time-evolution for both soot precursors and soot particles; however, the method used to depict each PSD will be different. We use the abbreviation of PSD to describe the distribution of soot precursors for convenience despite the size of precursors being too small to be considered particles.

The precursor PSD is represented using a sectional method. In the sectional method, a series of pseudo-chemical species are used to represent all precursors that are within a section of the full PSD. Each section is a subset of the PSD with different size ranges. The combination of all sections represents the entirety of the precursor PSD,

$$N_{total}^{PAH} = \sum_{i=0}^{n_{bins}} N_i^{PAH}, \tag{1}$$

where N_i^{PAH} is the number density of precursor molecules within a given section. Upper and lower bounds of each section were determined by molecular weight in this work, but can be determined by other indicators, such as collision diameter. N_i^{PAH} refers to all precursors within a given section, not just PAHs formed from light gases.

As the molecular weight range of the precursor PSD remains roughly fixed and sufficiently narrow (150-3500 g/mole), a sectional approach for representing the PSD is both accurate

and computationally affordable. On the other hand, the soot PSD range is not fixed and highly dependent on system configuration, sometimes growing to very broad ranges. Thus using a sectional approach to represent the PSD becomes increasingly difficult; the presented model uses the method of moments to represent the soot PSD. The method of moments involves the use of a set of statistical moments that describe a PSD,

$$M_r = \sum_{i=1}^{\infty} m_i^r N_i, \tag{2}$$

where M_r is the resolved rth moment, m_i is the molecular weight of particle i, and N_i is the number density of particles i. In theory, every discrete distribution can be described by a finite set of moments. However, in most cases a true soot PSD would require a set of moments well beyond computational possibility and so only a few moments are used; the more moments resolved, the more accurate the depiction of the true PSD. Validation cases presented in this study were limited to the resolution of 6 integer moments for the soot PSD [5].

Interpolative closure, as developed by Frenklach [5], was used to resolve all fractional moments needed by the model. Interpolative closure uses a Lagrangian interpolation between resolved whole moments to determine fractional moments that arise in the submodels used to describe the time evolution of the PSD moments. The Lagrangian interpolation is given by

$$\log M_p = L_p \left(\log M_0, \log M_1, ..., \log M_n\right), \tag{3}$$

$$L_p \left(\log M_0, \log M_1, ..., \log M_n\right) = \sum_{i=0}^{n} \log M_i \prod_{\substack{j=0 \\ j \neq i}}^{n} \frac{p-j}{i-j}. \tag{4}$$

Details for the time-resolution of each precursor section or soot moment used in this model are given below. For further details on model derivations and justifications refer to Appendix A.

2.1. Precursors

As mentioned above, the precursor PSD is represented by the sectional method. The rate of formation of each section's number density is determined by a series of submodels, written as

$$\frac{dN_i^{PAH}}{dt} = r_{form_i} - r_{nucl_i} - r_{depo_i} - r_{crack_i} + r_{growth_i} - r_{consume_i}, \tag{5}$$

where the r expressions represent the formation, soot nucleation, deposition, thermal cracking, surface growth, and consumption of each precursor section.

2.1.1. Precursor Formation

Precursors are formed in two ways: release from the parent fuel during primary pyrolysis, or molecular build-up from light gases,

$$r_{form_i} = R_{pyrene}\delta\left(m_{pyrene} - m_i\right) + R_{pyrolysis_i}. \tag{6}$$

PAH formation from light gas precursors, R_{pyrene}, is modeled using a gas-phase chemistry mechanism developed by Appel, Bockhorn, and Frenklach [4] (ABF mechanism), which details the production of pyrene, a common species used to model soot nucleation. The ABF mechanism can be implemented in Cantera, a suite of software tools for problems involving chemical kinetics, thermodynamics, and/or transport processes [20], or another similar software, and used to determine the production rate of pyrene in the gas-phase. The molecular weight of pyrene is 202.25 kg/kmol and contributes to the formation in only one PSD section; hence the delta function in the first term of Eq. 6.

Precursors released from the parent fuel, $R_{pyrolysis_i}$ in Eq. 6, are evolved directly into sections of the precursor PSD according to their molecular weight. Release rates need to be determined by methods outside the scope of this model but may either be modeled or taken from experimental data.

2.1.2. Soot Nucleation

Soot nucleation is modeled as the coalescence of two precursors to form a soot particle. This process removes the two precursors from the precursor PSD and adds a soot particle to the soot PSD represented by the soot moments. In terms of the precursor PSD, nucleation was given by Frenklach and Wang [10] as

$$r_{nucl_i} = \sum_{j=1}^{n_{bins}} \beta_{i,j}^{PAH} N_i^{PAH} N_j^{PAH}. \tag{7}$$

$\beta_{i,j}^{PAH}$ represents the frequency of collision between the two sectional species

$$\beta_{i,j}^{PAH} = 2.2\sqrt{\frac{\pi k_B T}{2\mu_{i,j}}}\left(d_i + d_j\right)^2, \tag{8}$$

$$\mu_{i,j} = \frac{m_i m_j}{m_i + m_j}, \tag{9}$$

$$d_i = C_h m_i^{1/2}, \tag{10}$$

$$C_h = d_A\sqrt{\frac{2}{3m_C}}, \tag{11}$$

where k_B is Boltzmann's constant, T is temperature, $\mu_{i,j}$ is the reduced mass of species i and j, d_i is the collision diameter of species i, d_A is the diameter of a single aromatic ring (0.28 nm), m_C is the mass of a single carbon atom (12.01 amu), and 2.2 is the van der Waals

enhancement factor, which accounts for the attraction of van der Waals forces as well as a collision efficiency [21, 22, 10].

The effect of nucleation on the soot PSD moments is expressed later in Section 2.2.1. Other mechanisms for soot nucleation have been proposed in the literature [23, 24, 25] and may be adapted to augment the currently proposed submodel.

2.1.3. Precursor Deposition

Soot growth via precursor deposition is modeled with the following precursor-soot collision rate,

$$r_{depo_i} = -\sum_{j=1}^{\infty} \beta_{i,j} N_j^{soot} N_i^{PAH}, \tag{12}$$

where $\beta_{i,j}$ is a collision frequency that includes the collision efficiency. Balthasar and Frenklach [26] expressed this model in terms of the precursor sizes and soot moments (derivation details are found in Appendix A.2)

$$r_{depo_i} = 2.2\sqrt{\frac{\pi k_B T}{2}} \left(C_h^2 m_i^{1/2} M_0^{soot} + 2C_h C_a C_s M_{1/3}^{soot} + C_s^2 C_a^2 m_i^{-1/2} M_{2/3}^{soot} \right) N_i^{PAH}. \tag{13}$$

Here, C_s and C_a are the spherical soot collision diameter and the particle shape deviation from spherical

$$C_s = \left(\frac{6}{\pi \rho_s} \right)^{1/3}, \tag{14}$$

$$C_a = (3 - 3\langle d \rangle) + (3\langle d \rangle - 2) C_{\langle d \rangle}, \tag{15}$$

where $\langle d \rangle$ is a shape factor related to the surface area of soot particles, detailed further in Section 2.2.4. $C_{\langle d \rangle}$ is a proportionality constant determined by a Monte-Carlo fitting to be 1.9125 [26].

2.1.4. Precursor Thermal Cracking

Thermal cracking is the chemical break-up of larger molecules, such as precursors, into lighter gases and is heavily influenced both by the chemistry of the molecule and temperature [27, 28]. In gaseous fuels, PAH molecules are made up of various aromatic rings, which are fairly stable and have only a small probability of thermally cracking. As more rings are added, forming soot particles, the molecule becomes more stable due to van der Waals forces, and eventually thermal cracking becomes negligible [29]. For complex solid fuels, precursors are mostly volatile tars released during primary pyrolysis. These tars are not completely made up of aromatic rings but rather contain aliphatic and non-carbon components, reflective of the parent fuel [30]. These inorganics and aliphatic groups make tars much more receptive to thermal cracking than gaseous-fuel PAHs [31].

Thermal cracking of the precursor PSD is represented using a model developed by Marias et al. [32]. In this model, tars are characterized as four basic types: phenol, toluene, naphthalene, and benzene. While the precursors are not actually phenol, toluene, naphthalene, or benzene, these four species are used as surrogates. In mathematical terms we may say 1

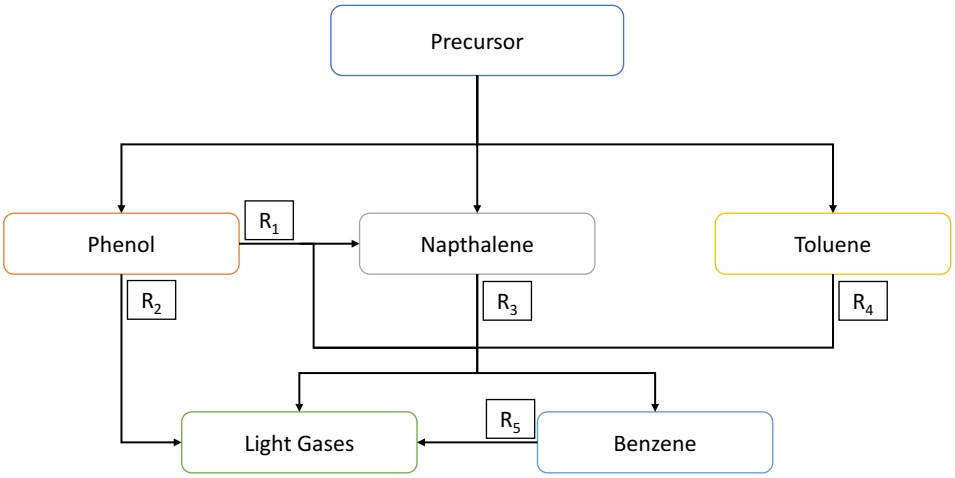

Figure 1: Basic outline of PAH thermal cracking.

mole of precursors is taken as 1 mole of a mixture of phenol, toluene, naphthalene, and benzene. Each of these types undergo different reactions, as mapped in Fig. 1. These reactions either convert one type to another with the difference of mass being released into the gas phase, or crack completely into lighter gases. The rates of each of these reactions are given in Table 1.

The Marias et al. model is translated into the number density change of precursor sections by multiplying the rates of reaction by the fraction of molecular weight cracked into light gas,

$$r_{crack_i} = \left(\frac{31.1}{94} k_1 x_{phe} + k_2 x_{phe} + \frac{50}{128} k_3 x_{napth} \left[H_2\right]^{0.4} + \frac{14}{92} k_4 x_{tol} \left[H_2\right]^{0.5} + k_5 x_{ben} \right) N_i^{PAH}, \quad (16)$$

where k_n values are given in Table 1. Details for this equation's derivation are given in Appendix A.3. $[H_2]$ is the concentration of H_2 measured in $\frac{kmole}{m^3}$. x_{phe}, x_{napth}, x_{tol}, and x_{ben} are the mole fractions of surrogate precursors. The difficulty in using this submodel lies in specifying the x_{phe}, x_{napth}, x_{tol}, and x_{ben} values. In this study, the fractions are taken as constant and the values are determined through a numerical study.

This numerical study was performed uniquely for each fuel/system considered. We evolve a representative group of precursors using the cracking scheme detailed in Table 1, at constant temperature and H_2 concentrations, until 98% of the precursors are fully converted to light gases. The time averaged mole fractions of the precursors are computed and used as constant values for x_{phe}, x_{napth}, x_{tol}, and x_{ben} in subsequent soot simulations. Temperature, H_2, and total initial precursor concentrations are set equal to peak system values as these values are a close representation of the conditions where thermal cracking occurs.

The initial precursor components are estimated as follows. We start with equal parts phenol, toluene, and naphthalene. But we want to maintain an initial aromatic/aliphatic carbon ratio reflective of the actual system. This is done by adding methyl groups to the toluene precursor components, thus during the numerical study the toluene components are

Table 1: Reactions and reaction rates used in precursor cracking scheme (rates in $\frac{kmole}{m^3 s}$, concentrations in $\frac{kmole}{m^3}$, and activation energies in $\frac{J}{mole\ K}$).

Reaction	Rates
$C_6H_6O \longrightarrow CO + 0.4\,C_{10}H_8 + 0.15\,C_6H_6 + 0.1\,CH_4 + 0.75\,H_2$	$R_1 = k_1[C_6H_6O]$ $k_1 = 1.00E7 \exp\left(\frac{-1.0E5}{RT}\right)$
$C_6H_6O + 3\,H_2O \longrightarrow 2\,CO + CO_2 + 3CH_4$	$R_2 = k_2[C_6H_6O]$ $k_2 = 1.00E8 \exp\left(\frac{-1.0E5}{RT}\right)$
$C_{10}H_8 + 4\,H_2O \longrightarrow C_6H_6 + 4\,CO + 5\,H_2$	$R_3 = k_3[C_{10}H_8][H_2]^{0.4}$ $k_3 = 1.58E12 \exp\left(\frac{-3.24E5}{RT}\right)$
$C_7H_8 + H_2 \longrightarrow C_6H_6 + CH_4$	$R_4 = k_4[C_7H_8][H_2]^{0.5}$ $k_4 = 1.04E12 \exp\left(\frac{-2.47E5}{RT}\right)$
$C_6H_6 + 5\,H_2O \longrightarrow 5\,CO + 6\,H_2 + CH_4$	$R_5 = k_5[C_6H_6]$ $k_5 = 4.40E8 \exp\left(\frac{-2.2E5}{RT}\right)$

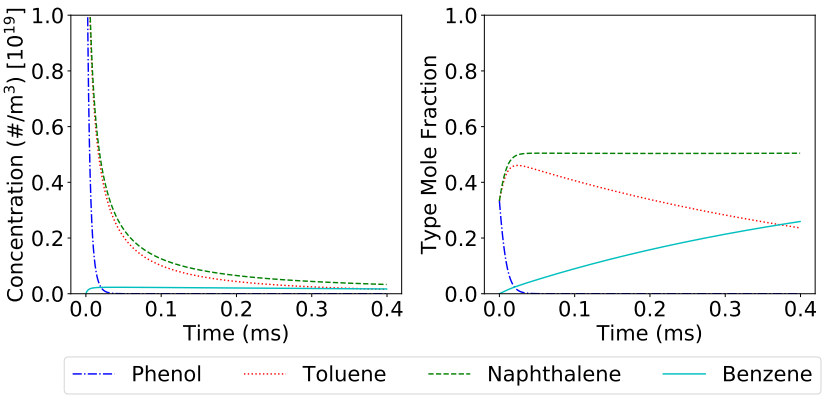

Figure 2: Result of numerical study considering the evolution of precursors from Pittsburgh #8 coal at 1800 K as found in Section 3.1. Results were 0.004, 0.283, 0.503, and 0.210 for x_{phe}, x_{napth}, x_{tol}, and x_{ben} respectively.

really polymethylbenzenes. To also maintain the given initial oxygen mass fraction, phenol groups are added to the phenol precursor components, thus during the numerical study the phenol components are really polyphenolicbenzenes. If the parent fuel is coal, the initial elemental composition and aromatic carbon fraction are the same as the parent coal. For biomass, the elemental compositions and aromatic carbon content were taken from Dufour et al. [33], which were 42.6% oxygen, 50.7% carbon, and 5.9% hydrogen; with 50% of the carbon as aromatic.

With an initialization of precursors with aromatic carbon ratios and oxygen mass fractions consistent with what would be found in the system precursors, we evolve these precursors in time according to the thermal cracking reactions. The precise reactions of Table 1 cannot be used in this exercise because the 'toluene' precursor component is not exactly toluene and the 'phenol' precursor component is not exactly phenol. The reactions in Table 1 need to be modified slightly to accommodate these differences. Reaction 4 is changed so that one methyl group is removed from the 'toluene' component per reaction (i.e., a trimethylbenzene would become a dimethylbenzene.) This means that only one reaction in every n reactions would produce benzene, where n is the number of methyl groups added to the toluene components to adjust the initial aromatic/aliphatic carbon ratio. Similar adjustments are made to reactions 1 and 2, where a single instance of reaction 1 or 2 only removes one OH group from the component until a true phenol is present. Then reactions 1 and 2 occur as shown in the table. Reactions 3 and 5 are unchanged.

Figure 2 shows the results of this numerical study as performed for Pittsburgh #8 coal at 1800 K, which is discussed later in Section 3.1.

2.1.5. Precursor Growth

Particles are able to either increase or decrease in mass through interactions with the surrounding gas phase. Increases in mass are modeled using the hydrogen abstraction and carbon addition (HACA) mechanism.

Details of the HACA mechanism have been carefully studied and validated [4, 34, 35, 36]. Concentrations of radical species are higher in a combustion environment, and these radical species, particularly $H^{\bullet}$, react with the particle surface abstracting a hydrogen atom, leaving a radical surface site. This radical site then reacts with acetylene in the surrounding gas, adding the acetylene's carbon to the surface. Another acetylene molecule is attached in the same way, completing an additional aromatic ring on the surface of the original particle and releasing another $H^{\bullet}$ into the surrounding gas. HACA is a self-sustaining chain reaction due to the number of radical species remaining constant throughout the mechanism. Figure 3 illustrates the addition of aromatic rings through the HACA mechanism. Kinetic rates for HACA are given in Table 2.

Each reaction rate given in Table 2 assumes a first order dependence on the gaseous species. The overall reaction rate (kg/m^2s) takes the form

$$R_{HACA} = 2m_C k_4 [\mathrm{C_2H_2}] \alpha \chi_{C^{\cdot}}. \tag{17}$$

$\chi_{C^{\cdot}}$ represents a number density of sites on the particle surface which have been radicalized. The α parameter is the fraction of those surface sites kinetically available for reaction. Early

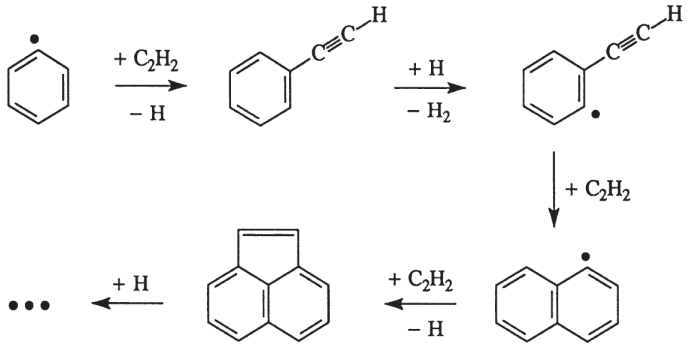

Figure 3: Diagram of the complete HACA mechanism illustrating growth of a benzene ring.

Table 2: Surface growth mechanism where $k_i = AT^n \exp\left(\frac{-E}{RT}\right)$ [4].

No.	Reaction	A $(\frac{m^3}{kmol \cdot s \cdot K^n})$	n	E $(\frac{J}{mole})$
1	$C{-}H + H^{\bullet} \longrightarrow C^{\bullet} + H_2$	4.2E10		54,392
1R	$C{-}H + H^{\bullet} \longleftarrow C^{\bullet} + H_2$	3.9E9		46,024
2	$C{-}H + OH^{\bullet} \longrightarrow C^{\bullet} + H_2O$	1.0E7	0.734	5,932
2R	$C{-}H + OH^{\bullet} \longleftarrow C^{\bullet} + H_2O$	3.68E5	1.139	7,093
3	$C^{\bullet} + H^{\bullet} \longrightarrow C{-}H$	2.0E10		
4	$C^{\bullet} + C_2H_2 \longrightarrow C{-}H + H^{\bullet}$	8.0E4	1.56	15,762

implementations of HACA used an α value of 1 due to a lack of data. Appel et al. [4], derived an empirical correlation for calculating α,

$$\alpha = \tanh\left(\frac{a}{\log \mu_1} + b\right), \tag{18}$$

where $\mu_1 = \frac{M_1}{M_0}$, and a and b are given as

$$a = 12.65 - 0.00563T, \tag{19}$$

$$b = -1.38 + 0.00068T. \tag{20}$$

The $\chi_{\mathrm{C}\cdot}$ value is computed using steady-state assumptions of the HACA mechanism in Table 2

$$\chi_{\mathrm{C}\cdot} = 2\chi_{\mathrm{C-H}}\frac{k_1[H] + k_2[OH]}{k_{-1}[\mathrm{H_2}] + k_{-2}[\mathrm{H_2O}] + k_3[H] + k_4[\mathrm{C_2H_2}]}. \tag{21}$$

$\chi_{\mathrm{C-H}}$ is the number density of sites on the particle surface available for reaction, estimated to be 2.3E19 sites/m^2 [4]. We note that, in addition to surface growth via acetylene in the HACA mechanism, there has been research suggesting an increasingly important role of propargyl to surface growth [37, 38, 39]. We have not found a generalized model for the addition of soot mass through propargyl and it has not been included here. In the results presented below, soot growth is dominated by tar-soot interactions.

The addition of mass to particles is accomplished by converting the mass added through HACA into an equivalent number of particles added to a PSD section

$$r_{growth_i} = \frac{R_{HACA} S_i^{PAH} N_i^{PAH}}{m_i}. \tag{22}$$

The surface area, S_i^{PAH}, of a precursor molecule is [40]

$$S_i^{PAH} = 5\mathrm{E}{-20} \cdot N_{C,i}^{PAH}, \tag{23}$$

$$N_{C,i}^{PAH} = \frac{m_i}{m_C}. \tag{24}$$

2.1.6. Precursor Consumption

We model the consumption of precursors via oxidation and gasification. Oxidation of a particle surface is an exothermic reaction between surface carbon/hydrogen atoms and oxidizing gases ($\mathrm{O_2}$ and OH here), leading to products of combustion: $\mathrm{CO_2}$, $\mathrm{H_2O}$, or CO [41, 42]. Gasification, on the other hand, is a less exothermic, possibly endothermic, reaction between a particle surface and gaseous molecules, such as $\mathrm{H_2O}$ or $\mathrm{CO_2}$, and results in a more diverse array of gaseous products which may include: products of combustion, small hydrocarbons, alcohols, carbonyls, and other species [43, 44].

The proposed model uses a global consumption submodel by Josephson et al. [45]. Oxidation and gasification rates (kg/m^2s) are given by

$$R_{oxidation} = \frac{1}{T^{1/2}}\left(A_{\mathrm{O_2}} P_{\mathrm{O_2}} \exp\left[\frac{-E_{\mathrm{O_2}}}{RT}\right] + A_{\mathrm{OH}} P_{\mathrm{OH}}\right), \tag{25}$$

Table 3: Parameters for surface consumption models found in Eqs. 25 and 26 [45].

Parameter	units	value	Equation
A_{O_2}	$\frac{kgK^{1/2}}{Pam^2s}$	1.92E-3	25
E_{O_2}	$\frac{J}{mol}$	1.16E5	25
A_{OH}	$\frac{kgK^{1/2}}{Pam^2s}$	2.93E-3	25
A_{CO_2}	$\frac{kg}{Pa^{1/2}K^2m^2s}$	1.92E-3	26
E_{CO_2}	$\frac{J}{mol}$	5.55E3	26
A_{H_2O}	$\frac{kgK^{1/2}}{Pa^nm^2s}$	1.92E-3	26
E_{H_2O}	$\frac{J}{mol}$	4.17E5	26

$$R_{gasification} = A_{\mathrm{CO_2}} P_{\mathrm{CO_2}}^{0.5} T^2 \exp\left[\frac{-E_{\mathrm{CO_2}}}{RT}\right] + A_{\mathrm{H_2O}} P_{\mathrm{H_2O}}^{1.21} T^{-1/2} \exp\left[\frac{-E_{\mathrm{H_2O}}}{RT}\right], \tag{26}$$

where reaction parameters are provided in Table 3. Both rates are mass consumption per unit surface area of the particles (kg/m^2s).

Similar to the growth term in Eq. 22, the consumption of particle number is accomplished by converting the mass consumed into an equivalent number of particles from a PSD section,

$$r_{consume_i} = \frac{\left(R_{oxidation} + R_{gasification}\right) S_i^{PAH} N_i^{PAH}}{m_i}. \tag{27}$$

2.2. Soot

As mentioned above, the soot PSD is represented using the method of moments. Moment rates are determined by a series of submodels,

$$\frac{dM_r}{dt} = Nu_r + Gr_r + Dp_r + Cg_r, \tag{28}$$

where the terms on the right-hand side of the equation represent nucleation, net surface growth (or consumption), precursor deposition, and particle coagulation.

2.2.1. Soot Nucleation

Nucleation of soot particles is accomplished through the coalescence of two precursor molecules. Section 2.1.2 describes the process of this coagulation and its effect on the precursor PSD. The expression for its effect on the soot PSD is similar [10],

$$Nu_r = \sum_{i=1}^{n_{bins}} \sum_{j=i}^{n_{bins}} \beta_{i,j} (m_i + m_j)^r N_i^{PAH} N_j^{PAH}, \tag{29}$$

where $\beta_{i,j}$ again represents the frequency of collision between precursor species i and j, it is computed using Eq. 8.

2.2.2. Soot Coagulation

Coagulation of soot particles is computed based on the collision frequency between soot particles [5]

$$Cg_r = \frac{1}{2}\sum_{k=1}^{r-1}\binom{r}{k}\left(\sum_{i=1}^{\infty}\sum_{j=1}^{\infty} m_i^k m_j^{r-k}\beta_{i,j}N_iN_j\right). \tag{30}$$

$\binom{r}{k}$ is the binomial coefficient. Note, that coagulation does not effect the first PSD moment, thus $Cg_1 = 0$.

The $\beta_{i,j}$ term, representative again of particle collision frequency, is dependent on the flow regime (continuum or free-molecular). The flow regime is classified by the Knudsen number, $Kn = 2\lambda_f/d$, where λ_f and d are the gas mean free path and average particle collision diameter, respectively. Model details and derivations are provided in Appendix A.4.

$\beta_{i,j}$ in the continuum flow regime is

$$\beta_{i,j}^C = K_C\left(m_i^{-1/3} + m_j^{-1/3} + K_C'\left[m_i^{-2/3} + m_j^{-2/3}\right]\right)(m_i^{1/3} + m_j^{1/3}), \tag{31}$$

leading to coagulation source terms in the continuum regime for $r = 0$ and $r \geq 2$,

$$Cg_0^c = -K_c[M_0^2 + M_{-1/3}M_{1/3} + K_c'(M_{-1/3}M_0 + M_{-2/3}M_{1/3})], \tag{32}$$

$$\begin{aligned} Cg_r^c = \frac{1}{2}K_c\sum_{k=1}^{r-1}\binom{r}{k}[&2M_kM_{r-k} + M_{k+1/3}M_{r-k-1/3} + M_{k-1/3}M_{r-k+1/3} \\ &+ K_c'(M_{k-1/3}M_{r-k} + M_kM_{r-k-1/3} + M_{k+1/3}M_{r-k-2/3} + M_{k-2/3}M_{r-k+1/3})], \end{aligned} \tag{33}$$

where the $K_c = 2k_BT/3\eta$ and $K_c' = 2.514\lambda_f/(C_sC_a)$, and η is the gas viscosity. C_s and C_a are evaluated using Eqs. 14 and 15. Fractional moments are computed using Lagrangian interpolation among logarithms of integer moments using Eq. 3.

Coagulation in the free molecular regime is more difficult as the $\beta_{i,j}$ expression is

$$\beta_{i,j}^f = K_f\left(m_i^{1/3} + m_j^{1/3}\right)^2\left(\frac{1}{m_i} + \frac{1}{m_j}\right)^{1/2}, \tag{34}$$

and results in a non-expandable form of summations in Eq. 30. Therefore, a grid function is established and evaluated using Lagrangian interpolation [5],

$$Cg_0^f = -\frac{1}{2}K_f f_{1/2}^{(0,0)}, \tag{35}$$

$$Cg_r^f = \frac{1}{2}K_f\sum_{k=1}^{r-1}\binom{r}{k}f_{1/2}^{(k,r-k)}, \tag{36}$$

where the $K_f = \epsilon C_a^2 C_s^2 \sqrt{\pi k_B T/2}$ and ϵ is the Van der Waals efficiency factor, taken as 2.2. The grid function $f_k^{(x,y)}$ is

$$f_k^{(x,y)} = \sum_{i=1}^{\infty}\sum_{j=1}^{\infty}\left(\frac{1}{m_i}+\frac{1}{m_j}\right)^k m_i^x m_j^y \left(m_i^{1/3}+m_j^{1/3}\right)^2 N_i N_j. \tag{37}$$

Fractional values of k needed to evaluate Eqs. 35 and 36 are computed using Lagrangian interpolation among the grid function evaluated at integer values of k [5]. An example of how to resolve these grid functions is given in Appendix A.6.

A weighted average of the coagulation source terms in the continuum and free-molecular regimes using the Knudsen number is used to compute the final soot coagulation source term

$$Cg_r = \frac{Cg_r^c}{1+Kn} + \frac{Cg_r^f}{1+1/Kn}. \tag{38}$$

2.2.3. Soot Surface Growth and Consumption

Just as the precursor PSD was affected by the growth or consumption of precursors through the interactions between a precursor's surface and the surrounding gas phase, the soot PSD also changes through the mechanisms previously discussed: HACA growth, oxidation, gasification, and precursor deposition. Details for the HACA, oxidation, and gasification were previously discussed in Sections 2.1.5 and 2.1.6. The rate of change of the number density of particle i is given by

$$\frac{dN_i}{dt} = \frac{k_s}{\Delta m}(N_{i-1}S_{i-1} - N_i S_i). \tag{39}$$

k_s is the rate of a surface reaction (HACA, oxidation, or gasification) and is equal to R_{HACA}, -$R_{oxidation}$, or -$R_{gasification}$ given in Eqs. 17, 25, and 26. Δm is the mass change to the particle due to a single reaction. For HACA, $\Delta m = 2m_C$, while for oxidation/gasification $\Delta m = m_C$. Applying moments, the net soot growth/consumption moment source term for $r \geq 1$ is derived to be

$$Gr_r = \pi C_s^2 \frac{k_s}{\Delta m} m_0^{2/3-\langle d\rangle} \sum_{k=0}^{r-1}\binom{r}{k}(\Delta m)^{r-k} M_{k+\langle d\rangle}. \tag{40}$$

For $r = 0$, $Gr_0 = 0$. Model details and derivations are given in Appendix A.5. Precursor deposition was discussed in Section 2.1.3 and the moment source term for $r \geq 1$ is

$$\begin{aligned} Dp_r = 2.2\sqrt{\frac{\pi k_B T}{2}} \sum_{k=0}^{r-1}\binom{r}{k} \big(C_h^2 M_{r-k+1/2}^{PAH} M_k^{soot} + 2C_h C_a C_s M_{r-k}^{PAH} M_{k+1/3}^{soot} \\ + C_s^2 C_a^2 M_{r-k-1/2}^{PAH} M_{k+2/3}^{soot}\big), \end{aligned} \tag{41}$$

where the C_h, C_s, and C_a constants were given in Eqs. 11, 14, and 15. For $r = 0$, we have $Dp_0 = 0$. The precursor PSD moment is calculated across all resolved sections

$$M_j^{PAH} = \sum_{i=1}^{n_{bins}} m_i^j N_i^{PAH}. \tag{42}$$

2.2.4. Soot Aggregation

Modeling soot aggregation deals directly the morphology of soot particles. As particles grow in size, particle morphology shifts from roughly spherical to aggregate chains. This behavior is modeled using the approach of Balthasar and Frenklach [26], in which an additional statistical moment is introduced which is related to the particle surface area. This moment, $M_{\langle d \rangle}$, is defined through the total particle surface area density, S,

$$S = S_0 \sum_{i=1}^{\infty} \left(\frac{m_i}{m_0} \right)^{\langle d \rangle} N_i = \frac{S_0}{m_0^{\langle d \rangle}} M_{\langle d \rangle}, \tag{43}$$

where S_0 and m_0 refer to the surface area and mass of an incipent soot particle upon nucleation. $\langle d \rangle$ is a shape factor, which can vary from 2/3, where the particles have the minimum possible surface area (spherical), to 1 , where particles have the maximum possible surface area (a chain of non-overlapping incipent particles). $\langle d \rangle$ is estimated using M_0, M_1, and $M_{\langle d \rangle}$,

$$\langle d \rangle = \frac{\log \mu_{\langle d \rangle}}{\log \mu_1}, \tag{44}$$

where $\mu_{\langle d \rangle} = \frac{M_{\langle d \rangle}}{M_0}$ and $\mu_1 = \frac{M_1}{M_0}$. While the introduction of $\langle d \rangle$ does not completely resolve the particle morphology, it can provide a particle collision diameter and surface area available for gas-surface reactions.

$M_{\langle d \rangle}$, the surface moment, is solved similar to other moments, with submodels for particle nucleation, precursor deposition, and net surface growth/consumption,

$$\frac{dM_{\langle d \rangle}}{dt} = Nu_{\langle d \rangle} + Dp_{\langle d \rangle} + Gr_{\langle d \rangle}. \tag{45}$$

The nucleation source, assuming spherical primary particles, is

$$Nu_{\langle d \rangle} = m_0^{2/3} Nu_0. \tag{46}$$

The deposition source term is determined by Lagrangian interpolation of the Dp_i terms for the resolved integer moments

$$Dp_{\langle d \rangle} = L_{\langle d \rangle} \left(\log Dp_1, \log Dp_2, \log Dp_3 \right). \tag{47}$$

Surface growth and consumption terms require the use of another grid function g_k. The source term is

$$Gr_{\langle d \rangle} = \pi C_s^2 \frac{k_s}{\Delta m} m_0^{2/3 - \langle d \rangle} \left(g_{\langle d \rangle} - M_{2\langle d \rangle} \right), \tag{48}$$

with details and derivations given in Appendix A.5. As in Eq. 39, k_s is the rate of a surface reaction (HACA, oxidation, or gasification) and is equal to R_{HACA}, -$R_{oxidation}$, or -$R_{gasification}$. Similar to $f_l^{(x,y)}$ in Eq. 37, g_k is computed at integer values and used to interpolate to $g_{\langle d \rangle}$. The grid function g_k needed in Eq. 48 is

$$g_k = \sum_{i=0}^{k} \binom{k}{i} \Delta m^{k-i} M_{i+\langle d \rangle}, \tag{49}$$

where Δm represents the mass of carbon change resulting from a single reaction ($\Delta m = 2m_C$ for HACA, and $\Delta m = m_C$ for oxidation and gasification).

In using this aggregation model, Balthasar and Frenklach [26] note that "constituent particles of the evolving aggregate are assumed to have point contacts with each other and, consequently, coagulation is assumed not to contribute to the change in the total surface area." Initially, this would imply that coagulation would not affect $M_{\langle d \rangle}$. However, a problem arises in coagulation dominated regions where M_1 and $M_{\langle d \rangle}$ remain stationary, but M_0 decreases. The decreasing number of particles pushes M_0 toward M_1 and $\langle d \rangle$ (computed from Eq. 44) decreases below its lower bound of 2/3.

To resolve this issue, we recognize $M_{\langle d \rangle}$ not as an absolute surface area moment, but rather on a scale between M_0 and M_1. Therefore, as particle coagulation affects one end of that scale, M_0, it must effect M_d as well. As the proposed submodel for particle coagulation in Section 2.2.2 is not designed to resolve fractional moments such as M_d, the equations are modified and Lagrangian interpolation is incorporated again using a grid function. Like the above coagulation scheme, submodels resolve the coagulation rate for both the free-molecular and continuum regimes. The continuum regime moment source term,

$$\begin{aligned} Cg^c_{\langle d \rangle} = K_c \Bigg(\frac{1}{2} h_{\langle d \rangle} - \big(& 2M_0 M_{\langle d \rangle} + M_{1/3} M_{\langle d \rangle - 1/3} + M_{-1/3} M_{\langle d \rangle + 1/3} \\ & + K'_C \left[M_0 M_{\langle d \rangle - 1/3} + M_{-2/3} M_{\langle d \rangle + 1/3} + M_{\langle d \rangle - 2/3} M_{1/3} + M_{-1/3} M_{\langle d \rangle} \right] \big) \Bigg), \end{aligned} \tag{50}$$

uses a grid function h_k in order to interpolate to $h_{\langle d \rangle}$ using Lagrange interpolation as before

$$\begin{aligned} h_k = \sum_{i=0}^{\infty} \sum_{j=0}^{\infty} (m_i + m_j)^k \Big(& 2 + m_i^{-1/3} m_j^{1/3} + m_i^{1/3} m_j^{-1/3} \\ & + K'_C \left[m_i^{-1/3} + m_i^{1/3} m_j^{-2/3} + m_i^{-2/3} m_j^{1/3} + m_j^{-1/3} \right] \Big) N_i N_j. \end{aligned} \tag{51}$$

Coagulation in the free-molecular regime,

$$Cg^f_{\langle d \rangle} = K_f \left(\frac{1}{2} f^{(0,0)}_{\langle d \rangle + 1/2} - f^{(\langle d \rangle, 0)}_{1/2} \right), \tag{52}$$

uses the grid function given in Eq. 37. Details and derivations are given in Appendix A.4 and a example of how to resolve grid functions is given in Appendix A.6.

Once the $Cg_{\langle d \rangle}$ is computed for both regimes, the results are weighted according to Eq. 38 above. This solution leads to an increased computational expense and the addition of the $Cg_{\langle d \rangle}$ term can be numerically stiff, but it is also accurate.

3. Validation

The proposed soot model has been implemented in several forms and the code have been verified. Included in the supplementary material is a coded rendition of this model written

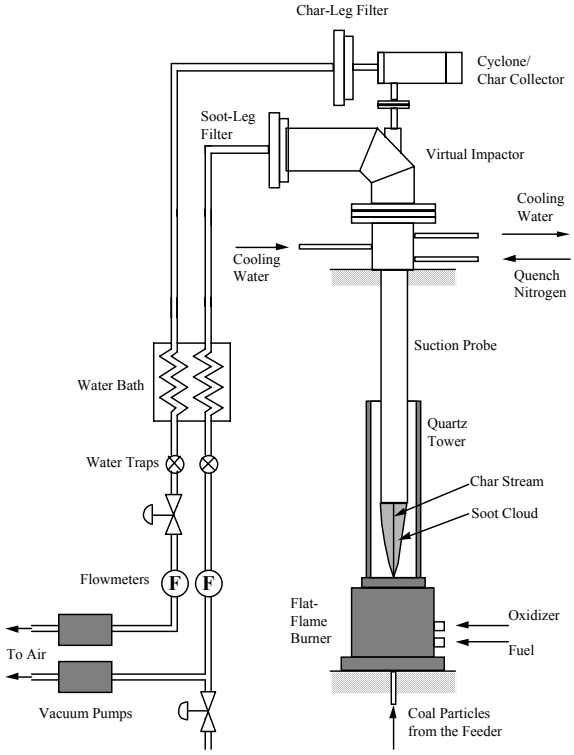

Figure 4: Diagram of flat flame burner used by Ma [12]. Reproduced with permission.

in Python. For validation of the proposed soot model, comparisons between model predicted and experimentally measured soot profiles were carried out for two different systems. The first system is a coal-fired laminar flat flame burner [46]. The second system is a biomass-fed gasifier [47]. Adequate data was published for both experiments to successfully reproduce the systems for simulation, allowing for model validation.

3.1. Coal System

Ma et al. [46, 12] collected soot from a coal-fired laminar flat flame burner, as depicted in Fig. 4. In this system, a Hencken flat-flame burner establishes a pre-mixed, fuel-lean laminar flame with in-flows of CH_4, H_2, and dilution N_2. Coal particles were steadily added to the center of the flame with an N_2 carrier gas. Proximate and ultimate analyses for three of the tested coals are summarized in Table 4.

The Hencken burner used is made up of a honey-comb mesh with small-diameter tubes inserted through the mesh-pores. Gases rapidly mix over the honeycomb and create a laminar flame sheet with a nearly uniform temperature profile [48, 49]. This particular burner was a square 5 cm on a side. Ma measured the spatial variation of temperature with a thermocouple at different heights and radial locations and found that within the inner 3 cm of the flame, temperatures varied radially by less than 40 K (about 2%) after the initial mixing layer (the first 2 cm above the burner.)

Table 4: Proximate and ultimate analyses for the six coals tested [46].

Coal Type	Moisture	Volatiles	Ash	C	H	N	S	O
Utah Hiawatha High-Volatile B Bituminous	7.58	38.78	9.14	80.53	5.96	1.33	0.47	11.71
Pittsburgh #8 High-Volatile A Bituminous	1.87	37.10	4.11	84.70	5.40	1.71	0.92	7.26
Illinois #6 High-Volatile A Bituminous	6.94	38.69	15.13	76.65	4.93	1.47	6.93	10.01

As particles entered the flame, primary pyrolysis occurred and particles devolatilized, resulting in precursors and lighter volatiles escaping into the gas phase, leaving a char particle behind. Volatile gases and char were collected by a nitrogen suction probe suspended at varying heights above the burner. This suction probe dilutes incoming gas with cool nitrogen through the walls of the probe, reducing the temperature of the collected sample to approximately 700 K at the mouth of the probe. Additional diluent nitrogen permeates the length of the probe walls to reduce sticking of particles on the inside of the probe.

From the probe, samples enter a virtual impactor where the momentum of heavier particles (char) carries them into a horizontal cyclone with a cut-off diameter of 5 μm. Particles with a larger diameter were collected in a char trap on the bottom of the cyclone, whereas smaller diameter particles passed through a soot filter at the top of the cyclone. In the virtual impactor, gases and small particles (soot) bend into a side arm. On this side arm is a soot filter through which gases pass. Gases from both the cyclone and the virtual impactor side arm pass through a water bath for cooling, water traps, flow meters, and other analysis equipment.

Data reported by Ma et al. included thermocouple readings along the flame centerline, with particle residence times at the same locations. Also reported were char, soot, and volatile yields from the suction probe collected along the flame centerline at varying heights. These soot yields were collected from two sources. The first source was from the two soot filters previously described, and these particles range in size from approximately 0.5-5.0 μm in diameter, as smaller particles would likely pass through the filter and larger particles ended up in the char collector. These larger particles were the second source of soot particles as they were separated from char using a sieve with 38 μm openings.

Soot particle sizes formed within the flame were on the order of 10-100 nm in effective diameter. However, agglomeration processes continued as particles were collected via the suction probe and passed through the probe, virtual impactor, side arm, and/or cyclone. Hence, particles grew from 10-100 nm at the collection probe to sizes captured by the soot filters.

3.1.1. Coal Simulations

As this system is both laminar and approximately one-dimensional, per the burner design, simulations replicating the environment for soot formation were computationally inexpensive and allowed for validation of the proposed soot model.

Simulations were carried out in one dimension for 120 mm along the gas flow direction. Ma [12] reported experimentally measured particle residence times at four locations for each coal type. These measurements were used to estimate instantaneous particle velocities. These particle velocity profiles, reported gas temperatures, and fuel properties (Table 4) were used with the Coal Percolation for Devolatilization (CPD) model [50] to predict particle devolatilization and the release of precursors during primary pyrolysis. As stated above, the soot model depends on an accurate prediction of soot precursors released from the parent fuel during primary pyrolysis. CPD can be modified to output a sectional size distribution of precursors during primary pyrolysis with section number and size dependent on coal type. These same sections were carried over to the precursor sectional model.

These simulations resolved the precursor PSD with 9 sections and the soot PSD with 6 statistical moments and a shape factor. Sections of the precursor PSD and moments of the soot PSD are transported in the z-direction by advection via the following the continuity equations

$$\frac{d(u_z N_i^{PAH})}{dz} = \frac{dN_i^{PAH}}{dt}, \tag{53}$$

$$\frac{d(u_z M_r)}{dz} = \frac{dM_r}{dt}, \tag{54}$$

assuming negligible axial diffusion relative to advection, and no significant pressure differential. Velocities, u_z, were interpolated among experimentally measured values and dz was kept constant at 1.2E-5 m, resulting in 10,000 steps per simulation.

Calculation of soot surface reaction rates for both PSDs requires species concentrations of C_2H_2, H, H_2,O_2, OH, CO_2, and H_2O. Chemical equilibrium at the local experimental temperature was assumed for these gas phase species using the ABF mechanism discussed in Section 2.1.1. The production rate of pyrene was computed from this gas state using the rate from the ABF mechanism, and any produced pyrene was added to the precursor PDF as described in Section 2.1.1. A soot cloud of 3 cm diameter was observed experimentally, and in simulation it was assumed that soot particle and chemical species concentrations were uniformly distributed across this cloud.

As described in Section 2.1.4 for the thermal cracking submodel, precursors were characterized as phenol, toluene, naphthalene, and benzene types. The mole fractions of these types is given in Table 5. The component fractions appear to vary more strongly with temperature than with coal type. For all species and temperatures, naphthalene fractions remain fairly constant. At higher temperatures toluene and phenol are exchanged for benzene. The precursor type fractions are arguably the only 'tunable' parameters for this simulation, but even these were not tuned to experimental data but rather computed as the expected time-evolution of the precursors in the system. This detailed model otherwise contained no parameters tuned to fit the experimental data.

Table 5: Precursor species fractions as described in Section 2.1.4 for the coal experiments.

Temp (K)	Coal	Mole Fraction			
		Phenol	Toluene	Naphthalene	Benzene
1650	Utah Hiawatha	0.008	0.424	0.508	0.067
1650	Pittsburgh #8	0.008	0.427	0.501	0.064
1650	Illinois #6	0.006	0.408	0.502	0.084
1800	Utah Hiawatha	0.004	0.277	0.503	0.216
1800	Pittsburgh #8	0.004	0.283	0.503	0.210
1800	Illinois #6	0.003	0.245	0.505	0.247
1900	Utah Hiawatha	0.003	0.198	0.505	0.294
1900	Pittsburgh #8	0.003	0.213	0.504	0.280
1900	Illinois #6	0.002	0.164	0.508	0.326

3.1.2. Coal Results

Ma reported soot collected from both filters and sieved from the char trap. These data are compared against the results of our simulations in Fig. 5. The plots in this figure display the yield of soot, as a mass percent of the parent coal, collected at different heights above the burner (which correlate to different particle residence times). The markers represent reported experimental results and the lines represent the simulations. Results are shown for three temperatures for each of the three coals. As can be seen in the figure, there is good agreement between experiments and simulations with regard to soot formation trends and locations. There is some disagreement between the magnitude of soot yield, but even this disagreement has reasonable error among soot prediction models [51]. The curve shapes found in the figure are indicative of reaction mechanisms but are consistent across all experiments. The total yield of soot is directly linked to the volatile yield of the parent fuel, as all three of these coals are high-volatile coals, all three have significant amounts of soot formed in their systems.

The location of soot formation is largely driven by the devolatilization rate of parent fuel. As the fuel devolatilizes, precursors are released into the system and immediately begin to nucleate or crack. The short time of soot mass build-up, occurring between 15 and 35 mm above the burner, seems to indicate that the life-span of these precursors in the flame is very short. In each of the cases, soot started to form approximately 15 mm above the burner. The higher temperature systems tend to form soot more quickly, but form less soot overall, compared to the lower temperature systems. This is because the higher temperatures force higher collision frequencies among precursors, thus increasing soot nucleation rates. These increases are offset by increased thermal cracking reaction rates, causing more precursor consumption and leading to an overall smaller soot yield.

Around 35 mm above the burner, all the precursors have been consumed and the soot yield levels off. Initially there is a slight, almost imperceptible drop in yield due to oxidation.

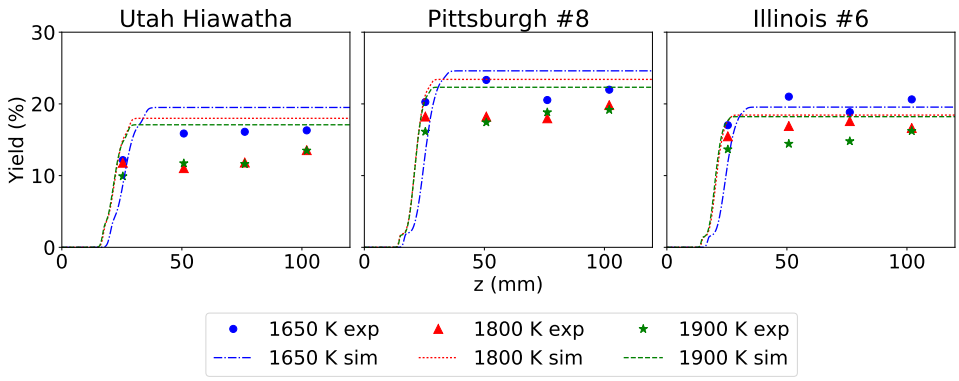

Figure 5: Simulation results, continuous dotted lines, are compared to reported experimental data, individual marks. Results are soot mass yield as a percent of original fuel mass (dry and ash free).

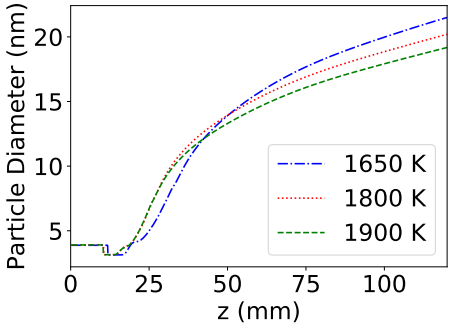

Figure 6: Average particle collision diameter across the flame portion of the Pittsburgh # 8 coal experiments.

This drop is most easily seen in the 1650 K Pittsburgh #8 experiment, but is present in all curves. Within the uptake of the flame was a small amount of oxygen which becomes OH, and it is this OH that begins to oxidize the soot. However, the OH is also consumed in oxidizing the soot particles, and is itself fully consumed before too long. C_2H_2, which causes surface growth, also is only present in small amounts and is fully consumed by the soot particles very quickly. Surface growth and consumption effects, like oxidation, are very small and are largely masked by soot nucleation in the initial mass build-up.

Note in Fig. 5 that the yield of the soot mass levels off around 25 to 35 mm above the burner for all cases. This is because in these low-temperature pre-mixed flames there is little to no pyrene or acetylene present in the chemistry of the system. This translates to very little particle mass increase due to gaseous growth of particles once the precursors released during primary pyrolysis are consumed. However, although no mass increase is occurring after the initial soot formation, this does not indicate that all mechanisms have stopped. Figure 6 shows the average particle collision diameter within the flame. The average particle size is continually increasing across the system as particles coagulate, changing the available

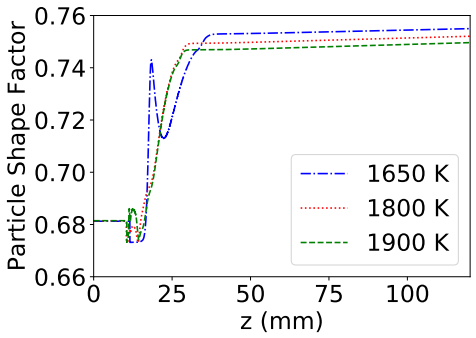

Figure 7: Particle shape factor across the flame portion of the Utah Hiawatha coal experiments.

particle surface area available for oxidation/gasification at the flame layer. This seems to indicate that particle size is strongly dependent on residence time and not only on mass yield.

Figure 7 shows that as the particle collision diameter grows the particles also become less spherical. Recall the description of the shape factor parameter $\langle d \rangle$ (as described in Section 2.2.4) indicates that at $\langle d \rangle = 2/3$ the particles are spherical but as $\langle d \rangle$ increases the particles become less spherical and have more surface area. Initially, as particle concentrations are very small, the profile is noisy as numerical errors dominate the computation of the shape factor. However, as particle concentrations increase there is an initial steep growth of the particle shape factor which quickly drops again. This trend is clearly evident in the 1650 K experiment but is present to a lesser extent in the other two experiments as well. This quick drop is the result of a slight amount of oxidation, which tends to round-out particles. There are not many oxidizing agents in this pre-mixed flame, but there are some, mostly OH, which quickly attack particle surfaces, consuming both agent and particle. The overall impact of this oxidation is hard to see in Fig. 5 but is much more evident in Fig. 7. After this initial oxidation we see the shape factor climb steeply once again until around 35 mm, at which point the precursors are fully consumed as described earlier. Once the precursors are consumed, the shape factor continues to climb but at a lesser rate. This steady climb is an indication of continued particle agglomeration throughout the flame, also seen in Figure 6. The combination of these two figures indicates that not only are particles growing in size, but are becoming more chain-like throughout the agglomeration-dominated region 35-50 mm above the burner.

In coal systems, tar is the dominant source of precursors and thus the dominant source of soot mass. An additional simulation of the burner without coal was done with soot precursors only coming from pyrene as described above. This simulation yielded soot mass less than 2% of the coal system. This shows an important quantity then is the amount of tar that is converted to soot. This value will be system dependent, but Fig. 8 reproduces Fig. 5 with a maximum sooting potential line included. These lines are an indication of the soot yield that would be observed if all tar molecules were converted to soot. As can be seen in the figure, not all tar molecules were nucleated to soot particles, the rest thermally

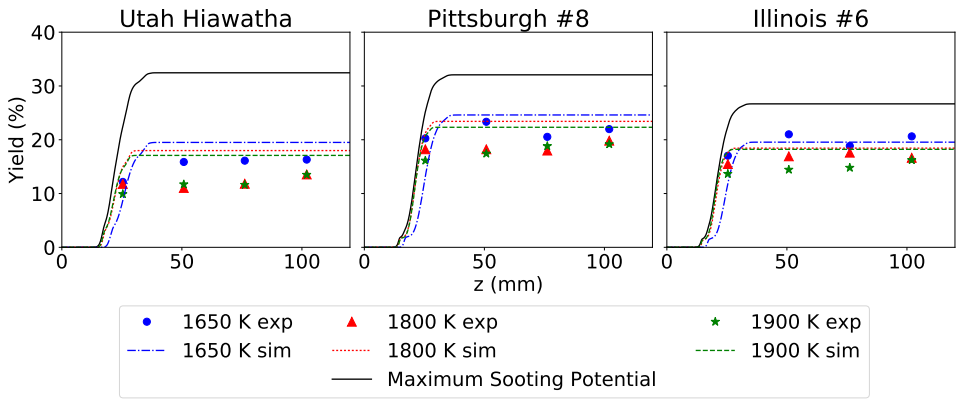

Figure 8: Soot mass yield with an additional 'maximum sooting potential' solid line representing the mass yield of tars released into the system.

cracked, oxidized, or were gasified. In the case of Utah Hiawatha: 61%, 56%, and 53% of the tar mass was converted to soot, dependent on temperature. For Pittsburgh #8: 78%, 73%, and 70% mass was converted. And for Illinois #6: 74%, 70%, and 69% mass was converted.

Experimental uncertainties were not reported, nor has a full uncertainty quantification for this model been done, so the precise discrepancy between the simulations and experiments is not known. Sources of error within the experiment nearly all lead to decreased collection of soot. The soot cloud was visually estimated by Ma to be around 3 cm while the opening to the suction probe was only 2.5 cm. This suction probe did have a vacuum applied to it which helped to collect most of the flame's soot cloud, but it is possible that some soot particles were not collected within the system. Additionally, small amounts of soot were known to deposit on the walls of the soot collection system, thus leading to reduced mass in measurements. Within the suction probe itself, nitrogen permeated the length of the probe walls to prevent particles sticking to the walls, but this permeating nitrogen was not consistent through the virtual impactor, injection tube, side arm, or cyclone. The soot filter pore size was 1 μm, but this filter is effective at capturing smaller particles as well; there were certainly particles that passed through the collection filters as a 1.0 μm collision diameter is a fairly large soot aggregate [52]. The cumulative effect of these uncertainties is difficult to quantify, but these uncertainties would result in the actual soot produced in the system being more than that reported. The simulation results consistently 'over-predicted' the measured soot concentrations within the system, and this is consistent with the sources of error. (The one exception to this is the 1650 K experiment with Illinois #6.) These results help to validate both the experiments and the proposed soot model for coal systems.

3.2. Biomass System

Trubetskaya et al. [47], collected soot from a fast-pyrolysis drop-tube reactor which gasified three types of biomass at two different temperatures, 1250 °C and 1400 °C. Biomass was fed into the reactor at a rate of ∼0.2 g min^{-1}, where it was rapidly heated and pyrolyzed

Table 6: Proximate and ultimate analyses for the biomass fuels tested.

Biomass Type	Moisture	Volatiles	Ash	C	H	N	S+Cl	O
Pinewood (Softwood)	5.1	86.6	0.3	53.1	6.5	.0.06	0.02	40.3
Beechwood (Hardwood)	4.5	79.4	1.4	50.7	5.9	0.13	0.04	43.3
Wheat Straw	5.5	77.5	4.1	46.6	6.1	0.6	0.2	46.5

Table 7: Precursor species fractions as described in Section 2.1.4 for the biomass experiments.

.

Temp (°C)	Biomass	Fraction			
		Phenol	Toluene	Naphthalene	Benzene
1250	Pinewood	0.157	0.415	0.424	0.004
1250	Beechwood	0.156	0.415	0.425	0.004
1250	Wheat Straw	0.152	0.417	0.427	0.004
1400	Pinewood	0.089	0.444	0.459	0.007
1400	Beechwood	0.088	0.445	0.460	0.007
1400	Wheat Straw	0.085	0.446	0.462	0.007

as it fell through the reactor. Reaction products were passed through a cyclone where larger particles (char and fly ash) were separated and fine particles (soot) were captured on a filter attached to the outlet of the cyclone [47, 53]. Proximate and ultimate analysis of the three biomass types are given in Table 6.

Collected particles were analyzed in a number of ways: elemental analysis, ash compositional analysis, FTIR spectroscopy, X-ray diffraction, thermogravimetric analysis, N_2 adsorption analysis, transmission electron microscopy (TEM), electron energy-loss spectroscopy, particle size distribution analysis, and graphitic structure. For purposes of validation, we focus here on the reported soot yield data and the particle size distribution analysis. Soot yield data were obtained for both an organic fraction and an inorganic fraction (through a standard ash test) of soot collected from the exhaust gas. However, in all cases soot was overwhelmingly organic, and inorganic fractions were only detectable in Wheat Straw soot and Beechwood soot at the higher temperature. The particle size distributions were estimated manually from TEM images. For every experiment, 50 particles were separated for the size analysis and every particle was assumed to spherical.

3.2.1. Biomass Simulations

In the simulations, we assumed that all soot was completely organic. Concentrations of precursors released during the primary-pyrolysis of the biomass were estimated using CPD-bio, an adaptation of CPD for estimating the behavior of biomass devolatilization using

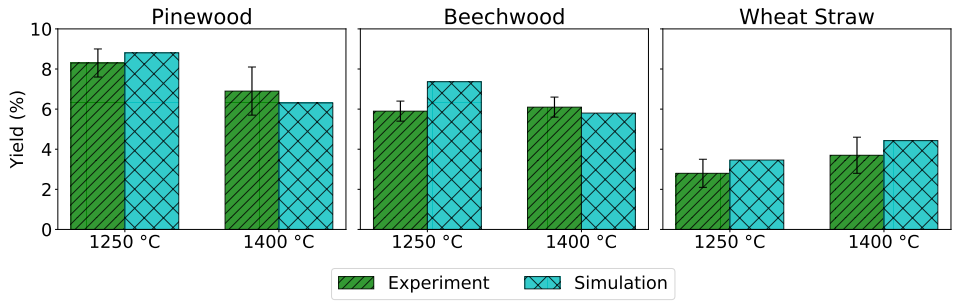

Figure 9: Results of coal-derived soot simulations compared to reported experimental data. Results are displayed as a mass percent of the parent fuel (dry and ash free).

the same structure principles derived for CPD [54]. Particle temperatures, velocities, and residence times were computed using the devolatilization model provided in the supplemental material of the original study [47]. These temperature profiles were then used in CPD-bio to predict tar yields segregated into a sectional precursor PSD. These simulations resolved the precursor PSD with 10 sections and the soot PSD with 6 statistical moments along with the shape factor.

Precursors were again characterized into different types and the results are shown in Table 7. Some trends we observed for coal seem to be consistent for biomass as well. There does not appear to be much difference in precursor type fractions between biomass species but there does seem to be a heavy correlation between the type fractions and temperature. Although there does not appear to be much variation between different biomass species, there is a significant difference between precursor type fractions for the biomass in Table 7 and type fractions for coal in Table 5.

Simulations assumed that chemical species and soot concentrations were uniform across the diameter of the reactor (2 cm) and chemical equilibrium using the ABF mechanism was assumed for gaseous species. We treated the soot formation simulation as a plug-flow reactor with Eqs. 53 and 54 solved for both precursor PSD sections and soot PSD moments.

3.2.2. Biomass Results

Figure 9 shows simulation results compared to the experimental data. As can be seen in the figure, there is good agreement between simulations and experiments with the simulation results all lying within or very close to the reported error bounds of the experiments; the only exception is the 1250 °C experiment for the Beechwood fuel. The model also captures the trends of the experiments, where higher temperatures generally led to higher rates of precursor thermal cracking, which led to lower soot yields, as seen in the Pinewood and Beechwood experiments. Soot yields from wheat straw, on the other hand, went up as the system responded the significant differences in the chemistry of the wheat straw, which was also captured by the model. In general, the softwood produces more soot than either the hardwood or the straw. This trend is seen in both experiments and in simulations, where again the only exception is the lower temperature hardwood.

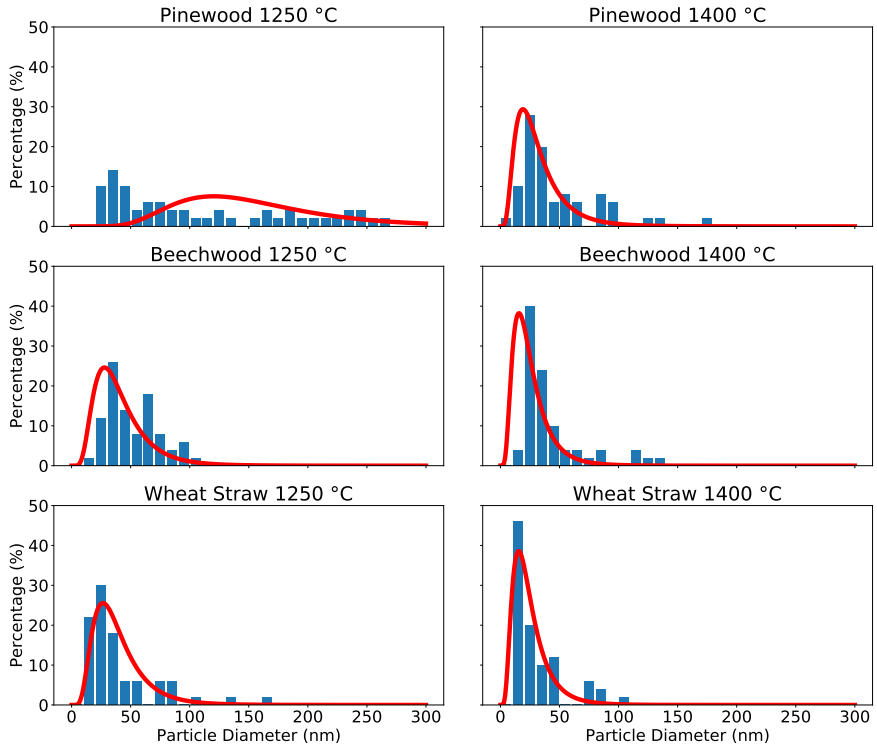

Figure 10: Blue bars represent experimentally measured particle-size distributions and red lines represent simulation resolved moments fitted to a log-normal distribution.

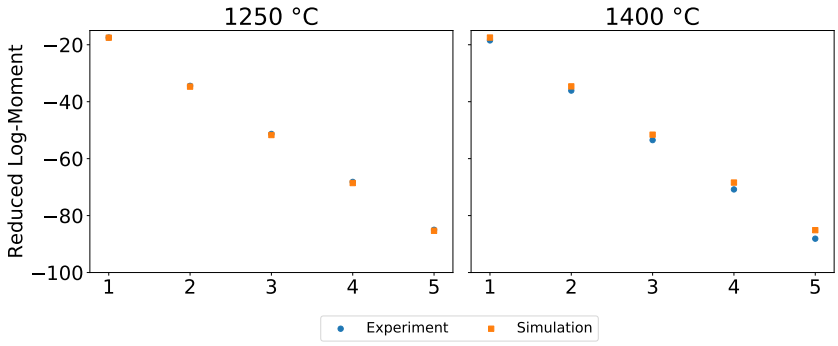

Figure 11: Log of reduced statistical moments for experiments and simulations for the Pinewood experiments at the two temperatures. Note that some experimental data points are obscured by their close proximity to the simulation data points.

The proposed detailed model does not resolve a full particle distribution but rather only moments of the distribution. In order to compare the experimentally analyzed distributions against the resolved statistical moments, the resolved moments were fitted to a log-normal distribution. With this assumption, a PSD could be reconstructed for each set of conditions and compared directly to available experimental data as seen in Fig. 10. In the experiments, 50 particles were analyzed for each set of conditions via visual analysis, and the results are seen as the blue bars of the figure. The red lines represent the first three simulation moments set to a log-normal distribution. While there certainly exist discrepancies between experimental data and simulation results, the two are highly complementary, with the exception of the 1250 °C Pinewood experiment. This experiment's difference may be due to the log-normal assumption used to reconstruct the distributions. This particular system had a much longer residence time than the others resulting in a flatter experimental distribution.

To compare experimental and simulation moments directly, we used reduced moments, that is $\mu_r = M_r/M_0$. Fig. 11 shows a direct comparison between these reduced moments for the Pinewood fuel. The other two experiments are almost identical in their comparison. Experimental and simulation moment orders never had an error of more than 6% , showing very good agreement for the particle distributions.

4. Conclusions

A physics-based model for predicting soot formation from solid-complex fuels was proposed. This model has a number of advantages for predictability in a wide variety of flames. Researchers should be comfortable extrapolating the use of this model without parameter calibration specific to their situation.

That being said, the model does not include every possible mechanism that can affect soot formation. For example, it is known from reported research [55, 47], that the presence of inorganics, Na, K, S, etc., in the soot particle structure can have catalytic effects on the chemical interactions between particle surface and surrounding gases. The exact effects of

these inorganics are not fully quantified or developed into a model form yet and thus not included here. While it is believed that catalytic effects are small, they are a source of error that researchers should be aware of, especially for biomass fuels which have a tendency to have more inorganics present.

In the model's current formulation, oxidation and gasification consume particle mass, which affects the higher moments of the soot PSD; however, it does not affect the zeroth moment, particle number density. As a result, when particles are fully consumed, simulation results may indicate a number of particles still present in the system where there is little or no mass. In addition, particles have a tendency to fragment [56, 57], whether through a mechanical breakage of an aggregate or through chemical consumption. Currently, this model does not account for any particle fragmentation.

Section 2.1.4 refers to the use of a submodel developed by Marias et al. [32] for predicting thermal cracking rates of soot precursors. This submodel requires a precursor characterization, and in this study we used time-averaged values for those precursor types determined by a numerical study described above. A numerical study done for every fuel type under unique conditions is undesirable and work is ongoing to improve aspects of this submodel's implementation. In addition, the total sensitivity of these type-fractions to overall soot yields is not completely quantified and also an area of ongoing model improvement.

The numerical economy of the Method of Moments applied in this model allows for detailed resolution of the soot PSD to be coupled with the resolution of other physics in reactive flows. However, even with these advantages the computational expense of the proposed model may be too high for use in large-scale simulations. This is because the full-detailed model presented contains multiple sections to be resolved for the precursor PSD and at minimum 4 moments to be resolved for the soot PSD with a large number of processes affecting each term. However, the detailed model presented is useful in calibrating simpler models for use in larger CFD simulations.

In conclusion, this proposed soot model shows promising results for predicting soot particle formation in a large variety of systems, but researchers using the model should be aware of implementation details and limits to tailor its use in their own systems. Work is ongoing to perform a full sensitivity analysis and uncertainty quantification of parameters found in the submodels of this proposed model. Both these analysis should help researchers understand the implications in implementing this model and variations of it into their simulations and own research.

5. Acknowledgements

This work was supported by the Department of Energy, National Nuclear Security Administration under Award DE-NA0002375, and by the United States Department of Agriculture Forest Service through the Rocky Mountain Research Station to develop an understanding of emissions formation in wildfires.

Appendix A. Model Derivations

This appendix is added to give greater details of some of the submodel derivations. This study uses the Method of Moments with Interpolative Closure (MoMIC), a commonly used model in the soot formation literature, but its derivation is not readily available. As a result, one may find multiple inconsistent variations of MoMIC among different research groups. One purpose of this Appendix is to provide a complete derivation for MoMIC which new researchers may use as a reference and as an aid to understanding the model.

Appendix A.1. Soot Nucleation from Sections 2.1.2 and 2.2.1

Soot nucleation is based on the coalescence of precursors

$$\frac{dN_i^{PAH}}{dt} = -\sum_{j=1}^{n_{bins}} \beta_{i,j}^{PAH} N_i^{PAH} N_j^{PAH}, \tag{A.1}$$

where $\beta_{i,j}$ represents the frequency that precursors N_i^{PAH} and N_j^{PAH} collide and stick together. The frequency factor $\beta_{i,j}^{PAH}$ is computed from collision theory

$$\beta_{i,j} = (d_i^{PAH} + d_j^{PAH})^2 \sqrt{\frac{\pi k_B T}{2\mu_{i,j}}}, \tag{A.2}$$

where k_B is Boltzmann's constant, T is the temperature, and $\mu_{i,j}$ is the reduced mass of precursors i and j

$$\mu = \frac{m_i m_j}{m_i + m_j}. \tag{A.3}$$

d_i^{PAH} represents the collision diameter of precursor i, which we compute using a geometric relationship for the most condensed PAH species of size m_i [10]

$$\begin{aligned} d_i^{PAH} &= d_A \sqrt{\frac{2m_i^{PAH}}{3m_C}}, \\ &= C_h \sqrt{m_i^{PAH}}, \end{aligned} \tag{A.4}$$

with d_A being the diameter of a single aromatic ring, $1.395\sqrt{3}$ Å.

Equation A.2 only describes the frequency of collision between two non-interacting spherical molecules. A van der Waals enhancement factor $\epsilon = 2.2$ [34, 58] is applied to Equation A.2, resulting in Equation 8.

Equation A.1 expresses the change in precursor sections' number densities due to soot nucleation. To evaluate the effect on the soot PSD we sum across all sections of the precursor PSD and divide by two to discount the double-counting of nucleation occurrences

$$\frac{dN}{dt} = \frac{1}{2} \sum_{i=1}^{n_{bins}} \sum_{j=1}^{n_{bins}} \beta_{i,j}^{PAH} N_i^{PAH} N_j^{PAH}. \tag{A.5}$$

Here N would indicate a soot particle the total number of soot particles. From here we can convolve the above equation with the moment definition, Equation 2, to obtain

$$\sum_{k=1}^{\infty} m_k^r \frac{dN}{dt} = \sum_{k=1}^{\infty} m_k^r \frac{1}{2} \sum_{i=1}^{n_{bins}} \sum_{j=1}^{n_{bins}} \beta_{i,j}^{PAH} N_i^{PAH} N_j^{PAH}. \tag{A.6}$$

Substitute $m_k = m_i^{PAH} + m_j^{PAH}$,

$$\sum_{k=1}^{\infty} m_k^r \frac{dN}{dt} = \sum_{k=1}^{\infty} \frac{1}{2} \sum_{i=1}^{n_{bins}} \sum_{j=1}^{n_{bins}} (m_i + m_j)^r \beta_{i,j}^{PAH} N_i^{PAH} N_j^{PAH}, \tag{A.7}$$

$$\sum_{k=1}^{\infty} m_k^r \frac{dN_k}{dt} = \frac{1}{2} \sum_{i=1}^{n_{bins}} \sum_{j=1}^{n_{bins}} (m_i + m_j)^r \beta_{i,j}^{PAH} N_i^{PAH} N_j^{PAH}, \tag{A.8}$$

$$\frac{dM_r}{dt} = \frac{1}{2} \sum_{i=1}^{n_{bins}} \sum_{j=1}^{n_{bins}} (m_i + m_j)^r \beta_{i,j}^{PAH} N_i^{PAH} N_j^{PAH}. \tag{A.9}$$

Which is equivalent to Equation 29.

Appendix A.2. Precursor Deposition from Sections 2.1.3, 2.2.3, and 2.2.4

The submodel for the precursor deposition, from the perspective of the precursors, begins the same as the nucleation submodel

$$\frac{dN_j^{PAH}}{dt} = -\sum_{i=1}^{\infty} \beta_{i,j} N_i N_j^{PAH}. \tag{A.10}$$

This equation represents the change of the number N_j^{PAH} of precursors as they collide and stick with N_i particles. The frequency factor $\beta_{i,j}$ is computed similar to Equation A.2, with a few small differences. We assume the mass m_i of the soot particle is much larger than the precursor molecule m_j. Therefore the reduced mass is $\mu_{i,j} = m_j$. We also substitute a soot particle diameter as this reaction occurs with the collision of a soot particle and precursor instead of two precursors

$$\beta_{i,j} = 2.2(d_i + d_j^{PAH})^2 \sqrt{\frac{\pi k_B T}{2m_j}}. \tag{A.11}$$

The diameter of the soot particle is a function of the particle mass and shape factor,

$$d_i = C_a C_s m_i^{1/3}, \tag{A.12}$$

where C_s, defined in Equation 14, is the coefficient related to the diameter of a spherical particle, and C_a, defined in Equation 15, is a coefficient relating to the particle shape deviation from spherical. Substitute this diameter definition back into Equation A.11

$$\beta_{i,j} = 2.2(C_a C_s m_i^{1/3} + C_h m_j^{1/2})^2 \sqrt{\frac{\pi k_B T}{2m_j}}, \tag{A.13}$$

$$\beta_{i,j} = 2.2\sqrt{\frac{\pi k_B T}{2}}(C_a^2 C_s^2 m_j^{-1/2} m_i^{2/3} + 2C_a C_s C_h m_i^{1/3} + C_h^2 m_j). \quad \text{(A.14)}$$

Substitute β back into Equation A.10

$$\frac{dN_j^{PAH}}{dt} = -2.2\sqrt{\frac{\pi k_B T}{2}} \sum_{i=1}^{\infty}(C_a^2 C_s^2 m_j^{-1/2} m_i^{2/3} + 2C_a C_s C_h m_i^{1/3} + C_h^2 m_j^{1/2}) N_i N_j^{PAH}, \quad \text{(A.15)}$$

and apply the definition of moments from Equation 2

$$\frac{dN_j^{PAH}}{dt} = -2.2\sqrt{\frac{\pi k_B T}{2}}(C_a^2 C_s^2 m_j^{-1/2} M_{2/3} + 2C_a C_s C_h M_{1/3} + C_h^2 m_j^{1/2} M_0) N_j^{PAH}, \quad \text{(A.16)}$$

which is the same as Equation 13.

To derive the effects of precursor deposition on the soot moments, we start by defining the change in the number of particles of a given size, m_i. The number of particles, N_i, increases as smaller particles, of size $m_i - m_j^{PAH}$, grow to m_i through the deposition process. N_i decreases as those particles grow larger also through deposition

$$\frac{dN_i}{dt} = \sum_{j=1}^{n_{bins}} \left(\beta_{i-j,j} N_{i-j} N_j^{PAH} - \beta_{i,j} N_i N_j^{PAH}\right). \quad \text{(A.17)}$$

We convolve Equation A.17 using the moment definition, Equation 2, to obtain

$$\sum_{i=1}^{\infty} m_i^r \frac{dN_i}{dt} = \sum_{i=1}^{\infty} m_i^r \sum_{j=1}^{n_{bins}} \left(\beta_{i-j,j} N_{i-j} N_j^{PAH} - \beta_{i,j} N_i N_j^{PAH}\right), \quad \text{(A.18)}$$

$$\frac{dM_r}{dt} = \underbrace{\sum_{i=1}^{\infty}\sum_{j=1}^{n_{bins}} m_i^r \beta_{i-j,j} N_{i-j} N_j^{PAH}}_{Term_1} - \underbrace{\sum_{i=1}^{\infty}\sum_{j=1}^{n_{bins}} m_i^r \beta_{i,j} N_i N_j^{PAH}}_{Term_2}. \quad \text{(A.19)}$$

Now we will treat each term individually. Discretize each PSD as a series of sections defined by the minimal possible size, m_C. When each is discretized, we can say that $m_i^r = i^r m_C^r$ (also note $m_j^r = j^r m_C^r$). Substitute this definition into the first term of A.19

$$Term_1 = \sum_{i=1}^{\infty}\sum_{j=1}^{n_{bins}} m_C^r i^r \beta_{i-j,j} N_{i-j} N_j^{PAH}. \quad \text{(A.20)}$$

Now we define $k = i - j$ and switch the order of the summations

$$Term_1 = \sum_{j=1}^{n_{bins}}\sum_{k=1-j}^{\infty} m_C^r (k+j)^r \beta_{k,j} N_k N_j^{PAH}. \quad \text{(A.21)}$$

There are no particles of negative or zero size, therefore we may set all portions of the summation where $k <= 0$ to be equal to zero

$$Term_1 = 0 + \sum_{j=1}^{n_{bins}} \sum_{k=1}^{\infty} m_C^r (k+j)^r \beta_{k,j} N_k N_j^{PAH}. \tag{A.22}$$

Substituting the binomial expansion of $(k+j)^r$ yields

$$Term_1 = \sum_{j=1}^{n_{bins}} \sum_{k=1}^{\infty} m_C^r \sum_{l=0}^{r} \binom{r}{l} j^{r-l} k^l \beta_{k,j} N_k N_j^{PAH}, \tag{A.23}$$

$$Term_1 = \sum_{j=1}^{n_{bins}} \sum_{l=0}^{r} \binom{r}{l} \sum_{k=1}^{\infty} \frac{j^r m_C^r k^l m_C^l}{j^l m_C^l} \beta_{k,j} N_k N_j^{PAH}. \tag{A.24}$$

$$Term_1 = \sum_{j=1}^{n_{bins}} \sum_{l=0}^{r} \binom{r}{l} \sum_{k=1}^{\infty} m_j^{r-l} m_k^l \beta_{k,j} N_k N_j^{PAH}, \tag{A.25}$$

Returning to Equation A.19, we substitute in the resolved value for the first term

$$\frac{dM_r}{dt} = \sum_{j=1}^{n_{bins}} \sum_{l=0}^{r} \binom{r}{l} \sum_{k=1}^{\infty} m_j^{r-l} m_k^l \beta_{k,j} N_k N_j^{PAH} - \sum_{i=1}^{\infty} \sum_{j=1}^{n_{bins}} m_i^r \beta_{i,j} N_i N_j^{PAH}. \tag{A.26}$$

Note, that when $r = l$ the first and second terms are equivalent. Therefore,

$$\frac{dM_r}{dt} = \sum_{j=1}^{n_{bins}} \sum_{l=0}^{r-1} \binom{r}{l} \sum_{i=1}^{\infty} m_j^{r-l} m_i^l \beta_{i,j} N_i N_j^{PAH}. \tag{A.27}$$

Now substitute the $\beta_{i,j}$ from Equation A.14, and simplify by using the definition of moments, Equations 2 and 42,

$$\frac{dM_r}{dt} = \sum_{j=1}^{n_{bins}} \sum_{l=0}^{r-1} \binom{r}{l} \sum_{i=1}^{\infty} m_j^{r-l} m_i^l 2.2 \sqrt{\frac{\pi k_B T}{2}} (C_a^2 C_s^2 m_j^{-1/2} m_i^{2/3} + 2 C_a C_s C_h m_i^{1/3} + C_h^2 m_j^{1/2}) N_k N_j^{PAH}, \tag{A.28}$$

$$\frac{dM_r}{dt} = 2.2 \sqrt{\frac{\pi k_B T}{2}} \sum_{l=0}^{r-1} \binom{r}{l} (C_a^2 C_s^2 M_{r-l-1/2}^{PAH} M_{l+2/3} + 2 C_a C_s C_h M_{r-l-1/2}^{PAH} M_{l+1/3} + C_h^2 M_{r-l+1/2}^{PAH} M_l), \tag{A.29}$$

to obtain Equation 41.

We can carry out this derivation for the soot surface moment but we will find that the fractional moments, M_d, leads to complications in the first term of Equation A.19. We can use a grid function to resolve that first term, but given the nature of this submodel it is simpler and computationally less expensive to resolve the submodel using Lagrangian Interpolation between the already resolved full moment terms as seen in Equation 47. In addition, this interpolation is just as accurate as applying a grid function to the first term of Equation A.19.

Appendix A.3. Precursor Cracking from Section 2.1.4

The entire principle behind the cracking scheme of this model is to take the Marias et al. model, that seen in Table 1, and apply it in way consistent with the sectional method of precursor evolution. We define the characterization of the precursor species

$$N_i^{PAH} = N_{i,Phenol} + N_{i,Naphthylene} + N_{i,Toluene} + N_{i,Benzene}, \tag{A.30}$$

$$N_{i,Phenol} = x_{phe} N_i^{PAH}, \tag{A.31}$$

$$N_{i,Naphthalene} = x_{napth} N_i^{PAH}, \tag{A.32}$$

$$N_{i,Toluene} = x_{tol} N_i^{PAH}, \tag{A.33}$$

$$N_{i,Benzene} = x_{ben} N_i^{PAH}, \tag{A.34}$$

where x_i represents a mole fraction of a precursor section that may be characterized by phenol, naphthalene, toluene, or benzene. The critical portion of this model is the use of phenol, naphthalene, toluene, and benzene directly as surrogates to represent those molecules

$$N_{i,Phenol} \approx N_{C_6H_6O}, \tag{A.35}$$

$$N_{i,Naphthalene} \approx N_{C_{10}H_8}, \tag{A.36}$$

$$N_{i,Toluene} \approx N_{C_7H_8}, \tag{A.37}$$

$$N_{i,Benzene} \approx N_{C_6H_6}. \tag{A.38}$$

The above equations may seem odd as the two species do not have the same mass, but it is important that we recognize that this approximation holds up with respect to how the species crack, as in that a single cracking reaction would result in a similar proportion of mass loss from the surrogate molecule and the actual precursor molecule and the rate of cracking reactions are approximately the same. Now working with just the surrogate in mind, we want to know the rate of mass cracked to gas for each surrogate species. Generalizing rates from Table 1, we may compute a rate of mass production for gas from the surrogate species

$$\dot{M}_{gas} = \sum m_i \nu R_i, \tag{A.39}$$

where ν is the stoichiometric coefficient associated with each gaseous species, positive if the species is a product and negative if it is a reactant. This equation only includes light gas

species, not any of the surrogate species; therefore, the first equation of Table 1 would only consider species CO, CH_4, and H_2. Recognizing now that the mass of gas produced is equal to the mass loss of surrogate species, we may convert that mass loss to an equivalent number of surrogate molecules consumed

$$\dot{M}_{gas} = \dot{M}_{surrogate}, \tag{A.40}$$

$$\frac{\dot{N}_{surrogate}}{N_a} \simeq \frac{\dot{M}_{surrogate}}{m_{surrogate}}. \tag{A.41}$$

The division of Avogadro's number is to convert kmoles to a number of molecules. Putting all this together for each reaction of the table,

$$\frac{dN_{C_6H_6O}}{N_a dt} = \frac{\left(m_{CO} + 0.1m_{CH_4} + 0.75m_{H_2}\right) k_1 \left[C_6H_6O\right]}{m_{C_6H_6O}}, \tag{A.42}$$

$$\frac{dN_{C_6H_6O}}{N_a dt} = \frac{\left(3m_{CO} + m_{CO_2} + 3m_{CH_4} - 3m_{H_2O}\right) k_2 \left[C_6H_6O\right]}{m_{C_6H_6O}}, \tag{A.43}$$

$$\frac{dN_{C_{10}H_8}}{N_a dt} = \frac{\left(4m_{CO} + 5m_{H_2} - 4m_{H_2O}\right) k_3 \left[C_{10}H_8\right] \left[H_2\right]^{0.4}}{m_{C_{10}H_8}}, \tag{A.44}$$

$$\frac{dN_{C_7H_8}}{N_a dt} = \frac{\left(m_{CH_4} - m_{H_2}\right) k_4 \left[C_7H_8\right] \left[H_2\right]^{0.5}}{m_{C_7H_8}}, \tag{A.45}$$

$$\frac{dN_{C_6H_6}}{N_a dt} = \frac{\left(5m_{CO} + m_{CH_4} + 6m_{H_2} - 5m_{H_2O}\right) k_5 \left[C_6H_6\right]}{m_{C_6H_6}}. \tag{A.46}$$

Combine Equations A.40 and A.41 as they both show the change of phenol. Now we take the approximation we set at the beginning of this derivation, $x_i N_i^{PAH} \approx N_i$ where i is a surrogate species and substitute into both sides of the above equations. Note that $[i] = \frac{N_i}{N_a}$,

$$\begin{aligned}\frac{d(x_{phe}N_i^{PAH})}{N_a dt} = &\frac{\left(m_{CO} + 0.1m_{CH_4} + 0.75m_{H_2}\right) k_1 \frac{\left(x_{phi}N_i^{PAH}\right)}{N_a}}{m_{C_6H_6O}} \\ &+ \frac{\left(3m_{CO} + m_{CO_2} + 3m_{CH_4} - 3m_{H_2O}\right) k_2 \frac{\left(x_{phi}N_i^{PAH}\right)}{N_a}}{m_{C_6H_6O}},\end{aligned} \tag{A.47}$$

$$\frac{d(x_{napth}N_i^{PAH})}{N_a dt} = \frac{\left(4m_{CO} + 5m_{H_2} - 4m_{H_2O}\right) k_3 \frac{\left(x_{napth}N_i^{PAH}\right)}{N_a} \left[H_2\right]^{0.4}}{m_{C_{10}H_8}}, \tag{A.48}$$

$$\frac{d(x_{tol}N_i^{PAH})}{N_a dt} = \frac{(m_{CH_4} - m_{H_2})\, k_4 \frac{\left(x_{tol}N_i^{PAH}\right)}{N_a} [H_2]^{0.5}}{m_{C_7H_8}}, \tag{A.49}$$

$$\frac{d(x_{ben}N_i^{PAH})}{N_a dt} = \frac{(5m_{CO} + 1m_{CH_4} + 6m_{H_2} - 5m_{H_2O})\, k_5 \frac{\left(x_{ben}N_i^{PAH}\right)}{N_a}}{m_{C_6H_6}}. \tag{A.50}$$

Conveniently, Avogadro's number would cancel out on both sides of each equation. Returning to Equation A.30, we substitute some values and take the derivative of both sides

$$\frac{dN_i^{PAH}}{dt} = \frac{d(x_{phe}N_i^{PAH})}{dt} + \frac{d(x_{napth}N_i^{PAH})}{dt} + \frac{d(x_{tol}N_i^{PAH})}{dt} + \frac{d(x_{ben}N_i^{PAH})}{N_a dt}, \tag{A.51}$$

substitute in our derived equations above, Equations A.47-A.50, and the known molecular weights and we get Equation 16 from the model.

Appendix A.4. Soot Coagulation from Sections 2.2.2 and 2.2.4

Similar to the collision between soot particles and precursors, the start of this model begins with two terms, the first representing the production of a given sized particle through the collision and sticking of two particles of lesser size, and the second representing the consumption of a given sized particle as it collides and sticks with another particle

$$\frac{dN_i}{dt} = \frac{1}{2}\sum_{j=1}^{i-1} \beta_{j,i-j} N_{i-j} N_j - \sum_{j=1}^{\infty} \beta_{i,j} N_i N_j. \tag{A.52}$$

Convolve this equation with the moment definition, Equation 2, to obtain

$$\sum_{i=1}^{\infty} m_i^r \frac{dN_i}{dt} = \sum_{i=1}^{\infty} m_i^r \left(\frac{1}{2}\sum_{j=1}^{i-1} \beta_{j,i-j} N_{i-j} N_j - \sum_{j=1}^{\infty} \beta_{i,j} N_i N_j \right), \tag{A.53}$$

$$\frac{dM_r}{dt} = \frac{1}{2}\sum_{i=1}^{\infty}\sum_{j=1}^{i-1} m_i^r \beta_{j,i-j} N_j N_{i-j} - \sum_{i=1}^{\infty}\sum_{j=1}^{\infty} m_i^r \beta_{i,j} N_i N_j. \tag{A.54}$$

If we iterate across the j parameter space first and then across the i space second, we can reorganize our iterization limits. Refer to Figure A.12 for a visual representation of this summation reorganization

$$\frac{dM_r}{dt} = \frac{1}{2}\sum_{j=1}^{\infty}\sum_{i=j+1}^{\infty} m_i^r \beta_{j,i-j} N_j N_{i-j} - \sum_{i=1}^{\infty}\sum_{j=1}^{\infty} m_i^r \beta_{i,j} N_i N_j. \tag{A.55}$$

Substitute, $k = i - j$, 2

$$\frac{dM_r}{dt} = \frac{1}{2}\sum_{j=1}^{\infty}\sum_{k+j=j+1}^{\infty} m_{k+j}^r \beta_{j,k} N_j N_k - \sum_{i=1}^{\infty}\sum_{j=1}^{\infty} m_i^r \beta_{i,j} N_i N_j, \tag{A.56}$$

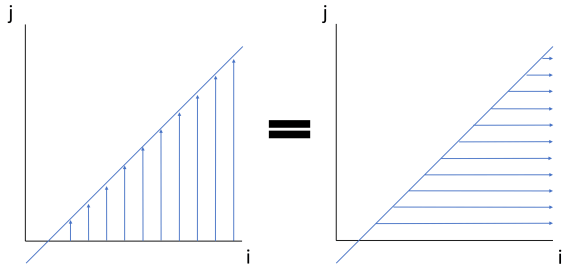

Figure A.12: Visual evidence of iteration reorganization.

$$\frac{dM_r}{dt} = \frac{1}{2}\sum_{j=1}^{\infty}\sum_{k=1}^{\infty}\left(m_k + m_j\right)^r \beta_{j,k} N_j N_k - \sum_{i=1}^{\infty}\sum_{j=1}^{\infty} m_i^r \beta_{i,j} N_i N_j. \tag{A.57}$$

Equation A.57 is the base equation common for all particle coagulation. From here we'll derive four different submodels: whole moment resolution for both continuum and free-molecular continuum flow regimes, and fractional moment resolution (for the surface moment) resolution in both regimes as well. First we will resolve the whole moment submodels. Through a binomial expansion we know that

$$\left(m_i + m_j\right)^r = \sum_{k=0}^{r}\binom{r}{k} m_i^k m_j^{r-k}. \tag{A.58}$$

Therefore

$$\frac{dM_r}{dt} = \frac{1}{2}\sum_{i=1}^{\infty}\sum_{j=1}^{\infty}\sum_{k=0}^{r}\binom{r}{k} m_i^k m_j^{r-k} \beta_{j,i} N_j N_i - \sum_{i=1}^{\infty}\sum_{j=1}^{\infty} m_i^r \beta_{i,j} N_i N_j. \tag{A.59}$$

Where $k = r$, the first term and second term are equivalent and cancel each other out

$$\frac{dM_r}{dt} = \frac{1}{2}\sum_{i=1}^{\infty}\sum_{j=1}^{\infty}\sum_{k=0}^{r-1}\binom{r}{k} m_i^k m_j^{r-k} \beta_{j,i} N_i N_j. \tag{A.60}$$

Now we resolve the frequency of coagulation parameter for the continuum regime, $\beta_{i,j}$, as defined by Seinfeld and Pandis [59]

$$\beta_{i,j}^C = K_C\left(\frac{C_i}{m_i^{1/3}} + \frac{C_j}{m_j^{1/3}}\right)\left(m_i^{1/3} + m_j^{1/3}\right), \tag{A.61}$$

$$K_C = \frac{2k_B T}{3\eta}, \tag{A.62}$$

$$C_i = 1 + 1.257Kn_i, \tag{A.63}$$

$$Kn_i = \frac{2\lambda_f}{d_i}, \tag{A.64}$$

$$d_i = C_a C_s m_i^{1/3}, \tag{A.65}$$

where k_B is Boltzmann's constant, T is the temperature, η is the gas viscosity, and λ_f is the gas mean free path, C_a and C_s were defined earlier in Equations 15 and 14 respectively. We substitute all these definitions back into Equation A.61 and then that back into Equation A.60,

$$\beta_{i,j}^C = K_C \left(\frac{1 + 1.257\frac{2\lambda_f}{C_a C_s m_i^{1/3}}}{m_i^{1/3}} + \frac{1 + 1.257\frac{2\lambda_f}{C_a C_s m_j^{1/3}}}{m_j^{1/3}} \right) \left(m_i^{1/3} + m_j^{1/3} \right), \tag{A.66}$$

$$K_C' = \frac{2.514\lambda_f}{C_a C_s}, \tag{A.67}$$

$$\beta_{i,j}^C = K_C \left(m_i^{-1/3} + m_j^{-1/3} + K_C' \left[m_i^{-2/3} + m_j^{-2/3} \right] \right) (m_i^{1/3} + m_j^{1/3}), \tag{A.68}$$

$$\begin{aligned} \frac{dM_r}{dt} = \frac{1}{2} \sum_{i=1}^{\infty} \sum_{j=1}^{\infty} \sum_{k=0}^{r-1} \binom{r}{k} m_i^k m_j^{r-k} K_C \Big(& m_i^{-1/3} + m_j^{-1/3} \\ & + K_C' \left[m_i^{-2/3} + m_j^{-2/3} \right] \Big) (m_i^{1/3} + m_j^{1/3}) N_i N_j, \end{aligned} \tag{A.69}$$

$$\begin{aligned} \frac{dM_r}{dt} = \frac{K_C}{2} \sum_{i=1}^{\infty} \sum_{j=1}^{\infty} \sum_{k=0}^{r-1} \binom{r}{k} \Big(& m_i^k m_j^{r-k} + m_i^{k+1/3} m_j^{r-k-1/3} + m_i^{k-1/3} m_j^{r-k+1/3} + m_i^k m_j^{r-k} \\ & + K_C' \left[m_i^{k-1/3} m_j^{r-k} + m_i^{k+1/3} m_j^{r-k-2/3} + m_i^{k-2/3} m_j^{r-k+1/3} + m_i^k m_j^{r-k-1/3} \right] \Big) N_i N_j, \end{aligned} \tag{A.70}$$

$$\begin{aligned} \frac{dM_r}{dt} = \frac{K_C}{2} \sum_{k=0}^{r-1} \binom{r}{k} \Big(& M_k M_{r-k} + M_{k+1/3} M_{r-k-1/3} + M_{k-1/3} M_{r-k+1/3} + M_k M_{r-k} \\ & + K_C' \left[M_{k-1/3} M_{r-k} + M_{k+1/3} M_{r-k-2/3} + M_{k-2/3} M_{r-k+1/3} + M_k M_{r-k-1/3} \right] \Big). \end{aligned} \tag{A.71}$$

This is equivalent to Equation 33, coagulation in the continuum flow regime. Sinc the binomial expansion of Equation A.58 does not hold when $r = 0$, we treat this case separately by deriving a simplified equation starting from Equation A.57

$$\frac{dM_0}{dt} = -\frac{1}{2}\sum_{j=1}^{\infty}\sum_{k=1}^{\infty}\beta_{j,k}N_jN_k, \tag{A.72}$$

substitute for $\beta_{i,k}$ from Equation A.61,

$$\frac{dM_0}{dt} = -\frac{1}{2}\sum_{j=1}^{\infty}\sum_{k=1}^{\infty}K_C\left(m_i^{-1/3} + m_j^{-1/3} + K'_C\left[m_i^{-2/3} + m_j^{-2/3}\right]\right)(m_i^{1/3} + m_j^{1/3})N_jN_k, \tag{A.73}$$

$$\frac{dM_0}{dt} = -K_C\left(M_0^2 + M_{1/3}M_{-1/3} + K'_C\left[M_0M_{-1/3} + M_{1/3}M_{-2/3}\right]\right). \tag{A.74}$$

Equivalent to Equation 32 coagulation in the continuum flow regime. Now we will resolve the frequency of coagulation parameter, $\beta_{i,j}$, in the free-molecular flow regime, again as defined by Seinfeld and Pandis [59]

$$\beta_{i,j}^F = (d_i + d_j)^2\sqrt{\frac{\pi k_B T}{2\mu_{i,j}}}, \tag{A.75}$$

$$\mu_{i,j} = \frac{m_i m_j}{m_i + m_j}. \tag{A.76}$$

Substitute definitions into Equation A.75 and then back into Equation A.60,

$$\beta_{i,j}^F = (C_aC_sm_i^{1/3} + C_aC_sm_j^{1/3})^2\sqrt{\frac{\pi k_B T}{2\frac{m_im_j}{m_i+m_j}}}, \tag{A.77}$$

$$\beta_{i,j}^F = C_a^2C_s^2\sqrt{\frac{\pi k_B T}{2}}(m_i^{1/3} + m_j^{1/3})^2\left(\frac{1}{m_i} + \frac{1}{m_j}\right)^{1/2}, \tag{A.78}$$

$$K_f = C_a^2C_s^2\sqrt{\frac{\pi k_B T}{2}}, \tag{A.79}$$

$$\frac{dM_r}{dt} = \frac{1}{2}\sum_{i=1}^{\infty}\sum_{j=1}^{\infty}\sum_{k=0}^{r-1}\binom{r}{k}K_f m_i^k m_j^{r-k}(m_i^{1/3} + m_j^{1/3})^2\left(\frac{1}{m_i} + \frac{1}{m_j}\right)^{1/2}N_iN_j. \tag{A.80}$$

This is equivalent to Equation 36 in the paper. As the term $(m_i^{1/3} + m_j^{1/3})^2$ cannot be expanded because of the fractional power, we use a grid function with Lagrangian interpolation

as described in the paper. An example of grid function resolution is shown later in Section Appendix A.6.

Resolving the surface moment's coagulation submodel is more difficult because of the fractional nature of the moment. The first term from Equation A.57 cannot be expanded because of the fractional exponential. Like before we use a grid function to resolve the first term of the equation after substituting the $\beta_{i,j}$ values for each regime, Equations A.61 and A.75, into the term. The grid functions to be resolved are $h_{\langle d \rangle}$ from Equation 51 for the continuum flow regime and $f^{0,0}_{\langle d \rangle}$ from Equation 37 for the free-molecular flow regime. Grid functions for these equations will not be expanded here and are left up to the reader, but an example of a grid function expansion is found in the following Section, Appendix A.6.

The second term can be expanded by substituting the $\beta_{i,j}$ values for each regime, Equations A.61 and A.75, into that term and resolving each into moment expressions. The end result can be seen in Equations 50 and 52 for the continuum and free-molecular flow regimes respectively.

Appendix A.5. Surface Reactions from Sections 2.2.3 and 2.2.4

This section refers to surface growth, via HACA, or surface consumption, via oxidation/gasification, as the derivation is the same for all these submodels. In each case, the model derivation is the same, differences only arise in the rate of reaction and the sign of the reaction. The starting point for our derivation deals once again with the number of molecules of a given size changing as molecules grow/shrink to that size and others grow/shrink beyond that size.

$$\frac{dN_i}{dt} = \frac{k_s}{\Delta m}\left(N_{i-1}S_{i-1} - N_i S_i\right), \tag{A.81}$$

k_s (kg/m^2 s) is the reaction rate per particle surface area and is unique to whichever process we are considering (HACA, oxidation, gasification), Δm is the change of mass due to a single reaction. Thus $\frac{k_s}{\Delta m}$ represents the number of reactions occurring per second and unit surface area of particles.

Convolve the definition of a moment, Equation 2, with Equation A.81

$$\sum_{i\,=1}^{\infty} m_i^r \frac{dN_i}{dt} = \sum_{i=1}^{\infty} \frac{m_i^r k_s}{\Delta m}\left(N_{i-1}S_{i-1} - N_i S_i\right), \tag{A.82}$$

$$\frac{dM_r}{dt} = \frac{k_s}{\Delta m}\left(\sum_{i=0}^{\infty} m_{i+1}^r S_i N_i - \sum_{i=1}^{\infty} m_i^r S_i N_i\right). \tag{A.83}$$

If we define the iterations of the sum to be in units of Δm, then $m_{i+1} = m_i + \Delta m$.

$$\frac{dM_r}{dt} = \frac{k_s}{\Delta m}\left(\sum_{i=0}^{\infty} (m_i + \Delta m)^r S_i N_i - \sum_{i=1}^{\infty} m_i^r S_i N_i\right), \tag{A.84}$$

$$\frac{dM_r}{dt} = \frac{k_s}{\Delta m}\left((m_0+\Delta m)^r S_0 N_0 + \sum_{i=1}^{\infty}(m_i+\Delta m)^r S_i N_i - \sum_{i=0}^{\infty} m_i^r S_i N_i\right), \quad \text{(A.85)}$$

$$\frac{dM_r}{dt} = \frac{k_s}{\Delta m}\left(\sum_{i=1}^{\infty}(m_i+\Delta m)^r S_i N_i - \sum_{i=1}^{\infty} m_i^r S_i N_i\right), \quad \text{(A.86)}$$

From our definition of $\langle d \rangle$, Equation 43, we can determine S, representing the surface area of all the particles, and thus S_i, the surface area of particle i,

$$S = \sum_{i=1}^{\infty} S_i N_i = S_0 \sum_{i=1}^{\infty}\left(\frac{m_i}{m_0}\right)^{\langle d \rangle} N_i, \quad \text{(A.87)}$$

$$S_i = S_0\left(\frac{m_i}{m_0}\right)^{\langle d \rangle}, \quad \text{(A.88)}$$

$$S_0 = \pi m_0^{2/3} C_s^2. \quad \text{(A.89)}$$

Substitute this surface area into Equation A.86

$$\frac{dM_r}{dt} = \frac{k_s}{\Delta m}\left(\sum_{i=1}^{\infty}(m_i+\Delta m)^r \pi m_0^{2/3} C_s^2\left(\frac{m_i}{m_0}\right)^{\langle d \rangle} N_i - \sum_{i=1}^{\infty} m_i^r \pi m_0^{2/3} C_s^2\left(\frac{m_i}{m_0}\right)^{\langle d \rangle} N_i\right). \quad \text{(A.90)}$$

Substitute the binomial expansion of $(m_i+\Delta m)^r$ into Equation A.90

$$\frac{dM_r}{dt} = \frac{k_s}{\Delta m}\left(\sum_{i=1}^{\infty}\sum_{k=0}^{r}\binom{r}{k}\Delta m^{r-k} m_i^k \pi m_0^{2/3} C_s^2\left(\frac{m_i}{m_0}\right)^{\langle d \rangle} N_i - \sum_{i=1}^{\infty} m_i^r \pi m_0^{2/3} C_s^2\left(\frac{m_i}{m_0}\right)^{\langle d \rangle} N_i\right). \quad \text{(A.91)}$$

When k=r, the first and second terms cancel out

$$\frac{dM_r}{dt} = \frac{k_s \pi C_s^2 m_0^{2/3-\langle d \rangle}}{\Delta m}\sum_{i=1}^{\infty}\sum_{k=0}^{r-1}\binom{r}{k}\Delta m^{r-k} m_i^{k+\langle d \rangle} N_i, \quad \text{(A.92)}$$

$$\frac{dM_r}{dt} = \frac{k_s \pi C_s^2 m_0^{2/3-\langle d \rangle}}{\Delta m}\sum_{k=0}^{r-1}\binom{r}{k}\Delta m^{r-k} M_{k+\langle d \rangle}, \quad \text{(A.93)}$$

which is equivalent to Equation 39.

To resolve the surface moment submodel we go back to Equation A.90,

$$\frac{dM_d}{dt} = \frac{k_s \pi C_s^2 m_0^{2/3-d}}{\Delta m} \left(\underbrace{\sum_{i=1}^{\infty} (m_i + \Delta m)^{\langle d \rangle} m_i^{\langle d \rangle} N_i}_{Term_1} - \underbrace{\sum_{i=0}^{\infty} m_i^{2\langle d \rangle} N_i}_{Term_2} \right), \tag{A.94}$$

in this equation, the second term resolves easily, but the first term cannot be expanded because of the fractional exponent. Once again we use a grid function, Equation 49, to resolve this term. With the introduction of the grid term, $g_{\langle d \rangle}$, and the resolution of the second term we get the equivalence of Equation 39.

Appendix A.6. Expansion of a grid function, Equation 37

We will expand the grid function for the soot coagulation among whole moments for the free-molecular flow regime as an example of how this grid function is used. This particular grid function is in reference to Equation 37 but the expansion process is the same for all grid functions used throughout this work.

Where $l = 0$,

$$f_0^{k,r-k} = \sum_{i=1}^{\infty} \sum_{j=1}^{\infty} \left(\frac{1}{m_i} + \frac{1}{m_j} \right)^0 m_i^k m_j^{r-k} (m_i^{1/3} + m_j^{1/3})^2 N_i N_j, \tag{A.95}$$

$$f_0^{k,r-k} = \sum_{i=1}^{\infty} \sum_{j=1}^{\infty} (m_i^{k+2/3} m_j^{r-k} + 2 m_i^{k+1/3} m_j^{r-k+1/3} + m_i^k m_j^{r-k+2/3}) N_i N_j, \tag{A.96}$$

$$f_0^{k,r-k} = (M_{k+2/3} M_{r-k} + 2 M_{k+1/3} M_{r-k+1/3} + M_k M_{r-k+2/3}). \tag{A.97}$$

Where $l = 1$,

$$f_1^{k,r-k} = \sum_{i=1}^{\infty} \sum_{j=1}^{\infty} \left(\frac{1}{m_i} + \frac{1}{m_j} \right)^1 m_i^k m_j^{r-k} (m_i^{1/3} + m_j^{1/3})^2 N_i N_j, \tag{A.98}$$

$$\begin{aligned} f_1^{k,r-k} = \sum_{i=1}^{\infty} \sum_{j=1}^{\infty} (& m_i^{k-1/3} m_j^{r-k} + 2 m_i^{k-2/3} m_j^{r-k+1/3} + m_i^{k-1} m_j^{r-k+2/3} + m_i^k m_j^{r-k-1/3} \\ & + 2 m_i^{k+1/3} m_j^{r-k-2/3} + m_i^{k+2/3} m_j^{r-k-1}) N_i N_j, \end{aligned} \tag{A.99}$$

$$\begin{aligned} f_1^{k,r-k} = & M_{k-1/3} M_{r-k} + 2 M_{k-2/3} M_{r-k+1/3} + M_{k-1} M_{r-k+2/3} \\ & + M_k M_{r-k-1/3} + 2 M_{k+1/3} M_{r-k-2/3} + M_{k+2/3} M_{r-k-1}. \end{aligned} \tag{A.100}$$

Where $l = 2$,

$$f_2^{k,r-k} = \sum_{i=1}^{\infty}\sum_{j=1}^{\infty}\left(\frac{1}{m_i}+\frac{1}{m_j}\right)^2 m_i^k m_j^{r-k}(m_i^{1/3}+m_j^{1/3})^2 N_i N_j, \tag{A.101}$$

$$\begin{aligned} f_2^{k,r-k} = \sum_{i=1}^{\infty}\sum_{j=1}^{\infty}(&m_i^{k-4/3}m_j^y + 2m_i^{k-5/3}m_j^{j+1/3} + m_i^{k-2}m_j^{r-k+2/3} + 2m_i^{k-1/3}m_j^{r-k-1} \\ &+ 4m_i^{k-2/3}m_j^{r-k-2/3} + 2m_i^{k-1}m_j^{r-k-1/3} + m_i^{k+2/3}m_j^{r-k-2} + 2m_i^{k+1/3}m_j^{r-k-5/3} \\ &+ m_i^k m_j^{r-k-4/3})N_i N_j, \end{aligned} \tag{A.102}$$

$$\begin{aligned} f_2^{k,r-k} = {} & M_{k-4/3}M_y + 2M_{k-5/3}M_{j+1/3} + M_{k-2}M_{r-k+2/3} + 2M_{k-1/3}M_{r-k-1} + 4M_{k-2/3}M_{r-k-2/3} \\ & + 2M_{k-1}M_{r-k-1/3} + M_{k+2/3}M_{r-k-2} + 2M_{k+1/3}M_{r-k-5/3} + M_k M_{r-k-4/3}. \end{aligned} \tag{A.103}$$

Where $l = 3$,

$$f_3^{k,r-k} = \sum_{i=1}^{\infty}\sum_{j=1}^{\infty}\left(\frac{1}{m_i}+\frac{1}{m_j}\right)^3 m_i^k m_j^{r-k}(m_i^{1/3}+m_j^{1/3})^2 N_i N_j, \tag{A.104}$$

$$\begin{aligned} f_3^{k,r-k} = \sum_{i=1}^{\infty}\sum_{j=1}^{\infty}(&m_i^{k-2/3}m_j^{r-k} + 2m_i^{8/3}m_j^{r-k+1/3} + m_i^{k-3}m_j^{r-k+2/3} + 3m_i^{k-4/3}m_j^{r-k-1} \\ &+ 6m_i^{k-5/3}m_j^{r-k-2/3} + 3m_i^{k-2}m_j^{r-k-1/3} + 3m_i^{k-1/3}m_j^{r-k-2} + 6m_i^{k-2/3}m_j^{r-k-5/3} \\ &+ 3m_i^{k-1}m_j^{4/3} + m_i^{k+2/3}m_j^{r-k-3} + 2_m i^{k+1/3}m_j^{r-k-8/3} + m_i^k m_j^{r-k-7/3})N_i N_j, \end{aligned} \tag{A.105}$$

$$\begin{aligned} f_3^{k,r-k} = {} & M_{k-2/3}M_{r-k} + 2M_{8/3}M_{r-k+1/3} + M_{k-3}M_{r-k+2/3} + 3M_{k-4/3}M_{r-k-1} \\ & + 6M_{k-5/3}M_{r-k-2/3} + 3M_{k-2}M_{r-k-1/3} + 3M_{k-1/3}M_{r-k-2} + 6M_{k-2/3}M_{r-k-5/3} \\ & + 3M_{k-1}M_{4/3} + M_{k+2/3}M_{r-k-3} + 2_m i^{k+1/3}M_{r-k-8/3} + M_k M_{r-k-7/3}. \end{aligned} \tag{A.106}$$

These four values, $f_0^{k,r-k}$,$f_1^{k,r-k}$,$f_2^{k,r-k}$, and $f_3^{k,r-k}$ are used with a Lagrangian interpolation scheme, Equations 3, along with their inter values, 0,1,2, and 3, to find $f_{1/2}^{k,r-k}$.

Appendix B. Nomenclature

Variable	Meaning	Units	Equations
A_{CO_2}	Pre-exponential constant for gasification via CO_2	$\frac{kgK^{1/2}}{Pa^{1/2}\cdot m^2\cdot s\cdot K^2}$	26
A_{H_2O}	Pre-exponential constant for gasification via H_2O	$\frac{kgK^{1/2}}{Pa^n m^2 s}$	26
A_{O_2}	Pre-exponential constant for oxidation via O_2	$\frac{kgK^{1/2}}{Pa\cdot m^2\cdot s}$	25
A_{OH}	Pre-exponential constant for oxidation via OH	$\frac{kgK^{1/2}}{Pa\cdot m^2\cdot s}$	25
C_a	Soot particle collision diameter constant	m	13, 15, 41
$C_{\langle d\rangle}$	Soot collision radius proportionality constant	—	15
C_h	Precursor collision diameter constant	m	10, 11, 13, 41
C_s	Soot particle spherical diameter	$\frac{m^{1/3}}{kg^{1/3}}$	13, 14, 40, 39, 41, 48
Cg_i	Rate at moment change due to coagulation	$\frac{kg^i}{s}$	28, 30, 32, 33, 35, 36, 38, 50, 52
Cn_i	Rate at moment change due to consumption	$\frac{kg^i}{s}$	28, 45
$\langle d\rangle$	Particle shape factor	—	15, 40, 43, 44, 45, 46, 47, 49 48, 50, 52
d_A	Diameter of a single aromatic ring	m	11
d_i	Collision diameter of species i	m	8, 10
Dp_i	Rate at moment change due to precursor deposition	$\frac{kg^i}{s}$	28, 41, 45, 47
E_{CO_2}	Activation energy for gasification via CO_2	$\frac{J}{mole}$	26
E_{H_2O}	Activation energy for gasification via H_2O	$\frac{J}{mole}$	26
E_{O_2}	Activation energy for oxidation via O_2	$\frac{J}{mole}$	25
$f_l^{(x,y)}, g_l, h_l,$	Grid functions defined within the text		35, 36, 37, 48, 49, 50, 51, 52

Gr_i	Rate at moment change due to surface growth	$\frac{kg^i}{s}$	28, 40, 45, 48
$[i]$	Concentration of species i	$\frac{kmol}{m^3}$	Table 1, 16, 17, 21
k_B	Boltzmann constant (1.38064852e-23)	$\frac{m^2kg}{s^2K}$	8, 13, 41, 47
k_s	Rate of a surface reaction	$\frac{kg}{m^2s}$	39, 40
K_c	Computed constant for the continuum regime of particle coagulation	$\frac{m^3}{s}$	31, 32, 33, 50, 51
K_c'	Another computed constant for the continuum regime of particle coagulation	$\frac{kg^{1/3}}{m^{1/3}}$	31, 32, 33, 50, 51
K_f	Computed constant for the free-molecule regime of particle coagulation	$\frac{m^3}{skg^{1/6}}$	34, 35, 36, 52
k_i	Kinetic rate constant	$\frac{m^3}{kmol \cdot s}$	Table 1, 17, 21
Kn	Knudsen number	—	38
m_i	Molecular mass of species i	kg	2, 6 ,9, 10, 11, 13, 17, 22, 24, 27, 29, 30, 31, 34, 37, 39, 40, 42, 43, 46, 48, 51
M_i	Moment i of a PSD	$\frac{kg^r}{m^3}$	2, 3, 4, 13, 28, 32, 33, 40, 41, 42, 43, 45, 48, 49, 50
n_{bins}	Number of resolved discrete sections	#	1, 7, 29, 42
N_i	Particles/molecules of species i	$\frac{\#}{m^3}$	1, 2, 5, 7, 13, 16, 22, 23, 24, 27, 29, 30, 37, 39, 42, 43, 51
Nu_i	Rate at moment change due to nucleation	$\frac{kg^i}{s}$	28, 29, 45, 46
P_i	Partial pressure of species i	Pa	25, 26
$r_{consume_i}$	Rate of oxidation/gasifcation for precursor species i	$\frac{\#}{m^3s}$	5, 27
r_{crack_i}	Rate of thermal cracking for precursor species i	$\frac{\#}{m^3s}$	5, 16

r_{depo_i}	Rate of deposition for precursor species i onto soot particles	$\frac{\#}{m^3 s}$	5, 13
r_{form_i}	Rate of formation for precursor species i	$\frac{\#}{m^3 s}$	5, 6
r_{growth_i}	Rate of surface growth for precursor species i	$\frac{\#}{m^3 s}$	5, 22
r_{nucl_i}	Rate of coagulation for precursor species i	$\frac{\#}{m^3 s}$	5, 7
R	Ideal gas constant	$\frac{J}{mole \cdot K}$	Table 1, 25, 26
R_{HACA}	Rate of surface growth through the HACA mechanism	$\frac{\#}{m^s s}$	17, 22, 39, 40, 48
$R_{gasification}$	Rate of gasification	$\frac{kg}{m^2 s}$	26, 27, 48
R_i	Reaction rate i	$\frac{\#}{m^s s}$	Table 1, Eq. 16
$R_{oxidation}$	Rate of oxidation	$\frac{kg}{m^2 s}$	25, 27, 48
R_{pyrene}	Rate of pyrene molecules created	$\frac{\#}{m^3 s}$	6
$R_{pyrolysis}$	Rate of precursor release from primary pyrolysis	$\frac{kg}{m^3 s}$	6
S_i	Surface area of species i	m^2	22, 23, 27, 39, 43
t	Time	s	5, 28, 39, 45
T	Local temperature	K	Table 1, 8, 13, 19, 20, 25, 26, 41, 47
x_{phe}, x_{naph}, x_{tol}, x_{ben}	Fraction of precursors characterized under a type	—	16
α	Fraction of surface sites kinetically available for reaction	—	17, 18
$\beta_{i,j}$	Frequency of collision between species i and j	$\frac{m^3}{s}$	7, 8, 29, 30, 31, 34
Δm	Change of mass resulting from a single reaction	kg	39, 40, 49
μ_i	Reduced moment i $\left(\frac{M_i}{M_0}\right)$	kg^i	18, 44
$\mu_{i,j}$	Reduced mass of species i and j $\left(\frac{m_i m_j}{m_i + m_j}\right)$	kg	8, 9
ρ_s	Soot density	$\frac{kg}{m^3}$	14
χ_i	Number of species i on particle surface	$\frac{\#}{m^2}$	17, 21

References

[1] S. Salenbauch, A. Cuoci, A. Frassoldati, C. Saggese, T. Faravelli, C. Hasse, Modeling soot formation in premixed flames using an Extended Conditional Quadrature Method of Moments, Combustion and Flame 162 (6) (2015) 2529–2543.

[2] H. Bockhorn, Soot formation in combustion: mechanisms and models, Springer-Verlag, Berlin ; New York, 1994.

[3] I. M. Kennedy, Models of soot formation and oxidation, Progress in Energy and Combustion Science 23 (2) (1997) 95–132.

[4] J. Appel, H. Bockhorn, M. Frenklach, Kinetic modeling of soot formation with detailed chemistry and physics: Laminar premixed flames of C-2 hydrocarbons, Combustion and Flame 121 (1-2) (2000) 122–136.

[5] M. Frenklach, Method of moments with interpolative closure, Chemical Engineering Science 57 (12) (2002) 2229–2239.

[6] S. J. Hong, M. S. Wooldridge, H. G. Im, D. N. Assanis, H. Pitsch, Development and application of a comprehensive soot model for 3D CFD reacting flow studies in a diesel engine, Combustion and Flame 143 (1-2) (2005) 11–26.

[7] H. Bockhorn, A. DAnna, Combustion Generated Fine Carbonaceous Particles: Proceedings of an International Workshop Held in Villa Orlandi, Anacapri, May 13 - 16, 2007, KIT Scientific Publishing, 2009.

[8] M. E. Mueller, G. Blanquart, H. Pitsch, Hybrid Method of Moments for modeling soot formation and growth, Combustion and Flame 156 (6) (2009) 1143–1155.

[9] M. Sirignano, J. Kent, A. D'Anna, Modeling Formation and Oxidation of Soot in Nonpremixed Flames, Energy & Fuels 27 (4) (2013) 2303–2315.

[10] M. Frenklach, H. Wang, Detailed Mechanism and Modeling of Soot Particle Formation, Soot Formation in Combustion 59 (1994) 165–192.

[11] M. Frenklach, H. Wang, O. Process, Aromatics Growth Beyond the First Ring and the Nucleation of Soot Particles, 202nd ACS National Meeting 36 (4) (1991) 1509–1509.

[12] J. Ma, Soot Formation During Coal Pyrolysis, Thesis, Brigham Young University, 1996.

[13] T. H. Fletcher, J. L. Ma, J. R. Rigby, A. L. Brown, B. W. Webb, Soot in coal combustion systems, Progress in Energy and Combustion Science 23 (3) (1997) 283–301.

[14] X. F. You, M. A. Gorokhovski, A. Chinnayya, A. Chtab, K. F. Cen, Experimental study and global model of PAH formation from coal combustion, Journal of the Energy Institute 80 (1) (2007) 12–21.

[15] D. Zeng, S. T. Hu, A. N. Sayre, H. Sarv, On the rank-dependence of coal tar secondary reactions, Proceedings of the Combustion Institute 33 (2) (2011) 1707–1714.

[16] A. L. Brown, T. H. Fletcher, Modeling soot derived from pulverized coal, Energy & Fuels 12 (4) (1998) 745–757.

[17] A. J. Josephson, D. O. Lignell, A. L. Brown, T. H. Fletcher, Revision to Modeling Soot Derived from Pulverized Coal (vol 12, pg 745, 1998), Energy & Fuels 30 (6) (2016) 5198–5199.

[18] A. Williams, M. Pourkashanian, J. M. Jones, Combustion of pulverised coal and biomass, Progress in Energy and Combustion Science 27 (6) (2001) 587–610.

[19] K. L. Xu, H. Zhang, Y. X. Wu, M. Baroncelli, H. Pitsch, Transient model for soot formation during the combustion of single coal particles, Proceedings of the Combustion Institute 36 (2) (2017) 2131–2138.

[20] D. G. Goodwin, H. K. Moffat, R. L. Speth, Cantera: An object- oriented software toolkit for chemical kinetics, thermodynamics, and transport processes, 2016.

[21] S. J. Harris, I. M. Kennedy, The Coagulation of Soot Particles with van der Waals Forces, Combustion Science and Technology 59 (4-6) (1988) 443–454.

[22] J. H. Miller, The kinetics of polynuclear aromatic hydrocarbon agglomeration in flames, Symposium (International) on Combustion 23 (1) (1991) 91–98.

[23] K. C. Lin, P. B. Sunderland, G. M. Faeth, Soot nucleation and growth in acetylene air laminar coflowing jet diffusion flames, Combustion and Flame 104 (3) (1996) 369–375.

[24] H. Wang, Formation of nascent soot and other condensed-phase materials in flames, Proceedings of the Combustion Institute 33 (2011) 41–67.
[25] Y. Matsukawa, K. Ono, K. Dewa, A. Watanabe, Y. Saito, Y. Matsushita, H. Aoki, K. Era, T. Aoki, T. Yamaguchi, Reaction pathway for nascent soot in ethylene pyrolysis, Combustion and Flame 167 (2016) 248–258.
[26] M. Balthasar, M. Frenklach, Detailed kinetic modeling of soot aggregate formation in laminar premixed flames, Combustion and Flame 140 (1-2) (2005) 130–145.
[27] K. R. Doolan, J. C. Mackie, R. J. Tyler, Coal Flash Pyrolysis - Secondary Cracking of Tar Vapors in the Range 870-2000 K, Fuel 66 (4) (1987) 572–578.
[28] M. A. Serio, W. A. Peters, J. B. Howard, Kinetics of Vapor-Phase Secondary Reactions of Prompt Coal Pyrolysis Tars, Industrial & Engineering Chemistry Research 26 (9) (1987) 1831–1838.
[29] R. A. Dobbins, Soot inception temperature and the carbonization rate of precursor particles, Combustion and Flame 130 (3) (2002) 204–214.
[30] F. Dabai, N. Paterson, M. Milian, P. Fennell, R. Kandiyoti, Tar Formation and Destruction in a Fixed Bed Reactor Simulating Downdraft Gasification: Effect of Reaction Conditions on Tar Cracking Products, Energy & Fuels 28 (3) (2014) 1970–1982.
[31] Y. B. Mao, Y. P. Dong, B. Wang, J. F. Chang, J. Yu, Y. Zhang, Y. Huo, C. S. Sun, Characteristics and kinetics of biomass tar cracking in a micro fluidized bed, Rsc Advances 5 (101) (2015) 82845–82852.
[32] F. Marias, R. Demarthon, A. Bloas, J. P. Robert-Arnouil, Modeling of tar thermal cracking in a plasma reactor, Fuel Processing Technology 149 (2016) 139–152.
[33] A. Dufour, E. Masson, P. Girods, Y. Rogaume, A. Zoulalian, Evolution of Aromatic Tar Composition in Relation to Methane and Ethylene from Biomass Pyrolysis-Gasification, Energy & Fuels 25 (9) (2011) 4182–4189.
[34] M. Frenklach, H. Wang, Detailed modeling of soot particle nucleation and growth, Symposium (International) on Combustion 23 (1) (1991) 1559–1566.
[35] R. S. Mehta, D. C. Haworth, M. F. Modest, An assessment of gas-phase reaction mechanisms and soot models for laminar atmospheric-pressure ethylene-air flames, Proceedings of the Combustion Institute 32 (2009) 1327–1334.
[36] J. Thomas Mckinnon, J. B. Howard, The roles of pah and acetylene in soot nucleation and growth, Symposium (International) on Combustion 24 (1) (1992) 965–971.
[37] C. F. Melius, J. A. Miller, E. M. Evleth, Unimolecular reaction mechanisms involving C3H4, C4H4, and C6H6 hydrocarbon species, Symposium (International) on Combustion 24 (1) (1992) 621–628.
[38] N. A. Slavinskaya, U. Riedel, S. B. Dworkin, M. J. Thomson, Detailed numerical modeling of PAH formation and growth in non-premixed ethylene and ethane flames, Combustion and Flame 159 (3) (2012) 979–995.
[39] A. Raj, M. J. Al Rashidi, S. H. Chung, S. M. Sarathy, PAH Growth Initiated by Propargyl Addition: Mechanism Development and Computational Kinetics, Journal of Physical Chemistry A 118 (16) (2014) 2865–2885.
[40] A. G. G. M. Tielens, The Physics and Chemistry of the Interstellar Medium, Cambridge University Press, Cambridge, 2005.
[41] K. G. Neoh, J. B. Howard, A. F. Sarofim, Soot oxidation in flames, book section 3, 261–28287, 1981.
[42] H. Guo, P. M. Anderson, P. B. Sunderland, Optimized rate expressions for soot oxidation by OH and O 2, Fuel 172 (2016) 248–252.
[43] Y. Chhiti, M. Peyrot, S. Salvador, Soot formation and oxidation during bio-oil gasification: experiments and modeling, Journal of Energy Chemistry 22 (5) (2013) 701–709.
[44] K. Leistner, A. Nicolle, P. Da Costa, Detailed Kinetic Analysis of Soot Oxidation by NO2, NO, and NO + O-2, Journal of Physical Chemistry C 116 (7) (2012) 4642–4654.
[45] A. J. Josephson, N. D. Gaffin, S. T. Smith, T. H. Fletcher, D. O. Lignell, Modeling Soot Oxidation and Gasification with Bayesian Statistics, Energy & Fuels 31 (10) (2017) 11291–11303.
[46] J. Ma, T. H. Fletcher, B. W. Webb, Conversion of coal tar to soot during coal pyrolysis in a post-flame environment, Twenty-Sixth Symposium (International) on Combustion, Vols 1 and 2 26 (2) (1996)

3161–3167.
[47] A. Trubetskaya, P. A. Jensen, A. D. Jensen, A. D. G. Llamas, K. Umeki, D. Gardini, J. Kling, R. B. Bates, P. Glarborg, Effects of several types of biomass fuels on the yield, nanostructure and reactivity of soot from fast pyrolysis at high temperatures, Applied Energy 171 (2016) 468–482.
[48] M. F. Campbell, G. A. Bohlin, P. E. Schrader, R. P. Bambha, C. J. Kliewer, K. O. Johansson, H. A. Michelsen, Design and characterization of a linear Hencken-type burner, Review of Scientific Instruments 87 (11).
[49] N. Kastelis, E. Zervas, Analysis of flat burners used to study gaseous pollutants emitted from combustion of hydrocarbons, Wwai '08: Proceedings of the 2nd International Conference on Waste Management, Water Pollution, Air Pollution, Indoor Climate (2008) 251–256.
[50] T. H. Fletcher, A. R. Kerstein, R. J. Pugmire, M. S. Solum, D. M. Grant, Chemical percolation model for devolatilization. 3. Direct use of carbon-13 NMR data to predict effects of coal type, Energy & Fuels 6 (4) (1992) 414–431.
[51] I. Glassman, Soot formation in combustion processes, Twenty-Second Symposium (International) on Combustion 22 (1988) 295–311.
[52] T. Mendiara, M. P. Domene, A. Millera, R. Bilbao, M. U. Alzueta, An experimental study of the soot formed in the pyrolysis of acetylene, Journal of Analytical and Applied Pyrolysis 74 (1-2) (2005) 486–493.
[53] B. Gktepe, K. Umeki, R. Gebart, Does distance among biomass particles affect soot formation in an entrained flow gasification process?, Fuel Processing Technology 141 (2016) 99–105.
[54] A. D. Lewis, T. H. Fletcher, Prediction of Sawdust Pyrolysis Yields from a Flat-Flame Burner Using the CPD Model, Energy & Fuels 27 (2) (2013) 942–953.
[55] M. P. Cal, B. W. Strickler, A. A. Lizzio, S. K. Gangwal, High temperature hydrogen sulfide adsorption on activated carbon II. Effects of gas temperature, gas pressure and sorbent regeneration, Carbon 38 (13) (2000) 1767–1774.
[56] A. Raj, R. Tayouo, D. Cha, L. Li, M. A. Ismail, S. H. Chung, Thermal fragmentation and deactivation of combustion-generated soot particles, Combustion and Flame 161 (9) (2014) 2446–2457.
[57] Q. Zhang, M. J. Thomson, H. Guo, F. Liu, G. J. Smallwood, Modeling of Oxidation-Driven Soot Aggregate Fragmentation in a Laminar Coflow Diffusion Flame, Combustion Science and Technology 182 (4-6) (2010) 491–504.
[58] K. M. Leung, R. P. Lindstedt, W. P. Jones, A Simplified Reaction-Mechanism for Soot Formation in Nonpremixed Flames, Combustion and Flame 87 (3-4) (1991) 289–305.
[59] J. H. Seinfeld, S. N. Pandis, Atmospheric Chemistry and Physics: From Air Pollution to Climate Change, vol. 2, John Wiley, New York, 2006.